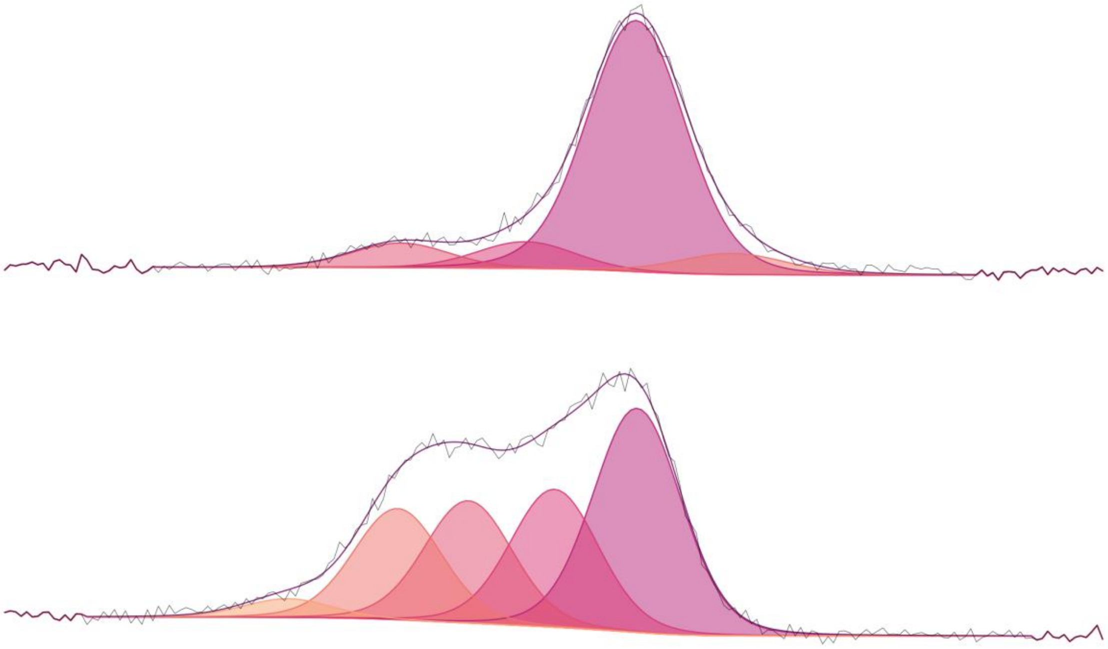

Investigating the role of electrode placement for operando AP-XPS battery studies

Master's thesis in Physics

Hanna Andersson

DEPARTMENT OF PHYSICS AND ASTRONOMY
CHALMERS UNIVERSITY OF TECHNOLOGY

Gothenburg, Sweden 2026
www.chalmers.se

MASTER'S THESIS

Investigating the role of electrode placement for operando AP-XPS battery studies

HANNA ANDERSSON

Department of Physics and Astronomy
CHALMERS UNIVERSITY OF TECHNOLOGY

Göteborg, Sweden 2026

Investigating the role of electrode placement for operando AP-XPS battery studies

HANNA ANDERSSON

Supervisor: Auðunn Orri Elvarsson
Examiner: Julia Maibach

Department of Physics and Astronomy

Chalmers University of Technology

SE-412 96,

Sweden

Cover: Two X-ray photoelectron spectroscopy spectra with fitted peaks.

Abstract

To enable the continued development of better batteries, it is crucial to improve the understanding of what happens inside the batteries during operation, especially at the electrode surfaces. For this, operando and in situ ambient pressure X-ray photoelectron spectroscopy (AP-XPS) battery studies have been utilized. However, these studies are performed in open beaker cells, where the electrodes are separated by ∼1 cm. Large separations between the electrodes has been found to result in distinct electrochemical behaviour of the cell compared to closely spaced electrodes in a coin cell. In this work, a new sample holder for AP-XPS at the HIPPIE beamline at MAX IV has been designed that places the electrodes side-by-side, only separated by ∼1 mm. This setup has then been compared to the currently used sample holder at HIPPIE, where the electrodes are placed 14 mm apart. The influence of these two electrode placements on electrochemical processes, surface composition, and resistances are investigated through in-house galvanostatic cycling, XPS and electrochemical impedance spectroscopy (EIS) experiments. This has been done by designing and 3D printing in-house sample holders that give the same electrode placement as those designed for the HIPPIE beamline. The electrodes of coin cells were also investigated to compare the performances of the beaker cells to a more more realistic commercial battery. The experiments were carried out on commercial lithium iron phosphate (LFP) and graphite battery electrodes, in a 1M $LiPF_6$ in ethylene carbonate/diethyl carbonate electrolyte. EIS measurement were carried out after the open-current voltage had stabilized, followed by a single galvanostatic charge-discharge cycle at C/10. XPS was then performed on cycled as well as on pristine electrodes. The results show differences in the electrochemical processes in the beaker cells compared to the coin cells, where the discharge capacity was smaller for the beaker cells indicating some irreversible reactions. Furthermore, the result also indicate that the resistances in the cells get larger when the distance between electrodes grows. While the electrode placement has a negligible affect on the surface composition of the LFP electrodes, the composition of the graphite electrodes varies substantially, with the largest difference still being between the coin cell and beaker cells. From this work, it can therefore be concluded that while the newly designed side-by-side electrode placement seems to reduce the overall cell resistances, it can't be concluded that there are any differences between the electrochemical performance and surface composition of the electrodes between the two beaker cells. Differences can however be seen for the electrochemical performance and surface composition of the graphite for the coin cells in comparison to the beaker cells. This is possibly explained by the large difference in electrolyte volume, rather than electrode placement. This work brings in situ AP-XPS studies a step closer to commercially relevant battery operation with the side-by-side electrode design and shows that there are differences between beaker cells and coin cells which should be considered when AP-XPS is performed.

Abbreviations

AP	Ambient pressure
CE	Counter electrode
CEI	Cathode electrolyte interphase
EIS	Electrochemical impedance spectroscopy
LIB	Lithium-ion battery
LFP	Lithium iron phosphate
RE	Reference electrode
RSF	Relative sensitivity factor
SEI	Solid electrolyte interphase
UHV	Ultra-high vacuum
WE	Working electrode
XPS	X-ray photoelectron spectroscopy

Contents

1 Introduction 1

2 Lithium-Ion Batteries 3
- 2.1 Battery Operation 3
- 2.2 The Solid Electrolyte Interphase 4

3 X-ray Photoelectron Spectroscopy on Batteries 6
- 3.1 X-ray Photoelectron Spectroscopy 6
- 3.2 Ambient Pressure XPS 8
- 3.3 Dip-and-Pull Experiments on Batteries 9

4 Experimental Setup and Materials 12
- 4.1 Design of Sample Holder 12
- 4.2 Materials 12
- 4.3 In-house Experimental Setup 13
  - 4.3.1 Beaker Cells 13
  - 4.3.2 Coin Cells 14

5 Experimental Methods 16
- 5.1 Galvanostatic Cycling 16
- 5.2 Electrochemical Impedance Spectroscopy 17
- 5.3 X-ray Photoelectron Spectroscopy 17

6 Results and Discussion 19
- 6.1 Galvanostatic Cycling 19
- 6.2 Electrochemical Impedance Spectroscopy 21
- 6.3 X-ray Photoelectron Spectroscopy 22

7 Conclusion and Outlook 31

A Supplementary Information 38
- A.1 Galvanostatic cycling 38
- A.2 Electrochemical Impedance Spectroscopy 40
- A.3 X-ray Photoelectron Spectroscopy 41

Chapter 1

Introduction

During the past decades, the global electricity consumption has steadily increased and has now reached well over 20 000 TWh a year [1]. Most of this electricity comes from the burning of fossil fuels [2]. This causes carbon, that was previous trapped in the earths crust, to be emitted as CO_2 in our atmosphere. In turn, the increase of CO_2 in our atmosphere drives the climate change we are witnessing [3], [4].

To eliminate the need for fossils fuel and stop the emission of CO_2, more renewable energy sources, like wind and solar power, must be utilized for the electricity generation. However, these renewable sources come with challenges. Renewable energy sources are not dispatchable, meaning that these energy sources can't provide energy on demand. For example, wind turbines can only generate electricity when it is windy and solar panels can only generate electricity when it is sunny. To solve this, and allow the share of electricity generation from renewable sources to expand, better ways of storing electrical energy for later use are required.

One technology that can be used to store energy is batteries. Batteries can convert electricity to chemical energy when the generation of renewable electricity is higher than the demand. When the demand instead is higher than the generation, the chemical energy can be converted back to electricity. The batteries of today are however accompanied with challenges like capacity loss and thermal runaways. By improving the performances of batteries, the storage of renewable energy can be made more effective and safer in the future.

To develop batteries with improved performances, a deeper understanding of the batteries of today are required. One part of the battery that has a large impact of the performance and property of the battery is the solid electrolyte interface (SEI) - a thin layer of decomposed electrolyte between the negative electrode and the electrolyte. An improved understanding of the composition and formation of the SEI and how this in turn affect the performance of batteries would be able to guide the development of new batteries.

A technique that can be used to probe and analyse the SEI is ambient pressure X-ray photoelectron spectroscopy (AP-XPS). This technique allows for dip-and-pull experiments, where the electrodes are placed in an open configuration, usually ~1 cm apart. For these experiments, the electrodes are dipped down in a beaker of electrolyte. The electrodes can then be pulled up from the electrolyte slightly, creating a meniscus that can be probed using AP-XPS. However, this configuration only allow for probing of one electrode due to the separation of the electrodes. Furthermore, concerns regarding how representative these cells are of realistic batteries, where the electrodes are pressed together with just a thin separator in-between, are raised.

This thesis focuses on developing and testing a new setup that allows for probing of both the positive and negative electrode using operando AP-XPS. This will be done by altering the electrode placement in so called dip-and-pull experiments to allow for probing of both the positive and negative electrode. The different cell configurations will then be studied to see how the electrode placement affects the performance and resistance of the cell as well as the surface compositions of the electrodes. The aim is to design a new sample holder, with a side-by-side electrode placement, for the HIPPIE beamline at MAX IV and answer the following research questions:

- How does the performance of an operando AP-XPS battery cell changes when the electrodes are placed side-by-side as opposed to 14 mm apart? How does these performances compare to the performance of a coin cell?
- How does the resistances in an operando AP-XPS battery cell change when the electrodes are placed 14 mm apart and side-by-side respectively? How does these resistances compare to the resistances in a coin cell?
- How does the chemical composition of the surface on the electrodes in an operando AP-XPS battery cell changes when the electrodes are placed 14 mm apart and side-by-side respectively? How does these chemical compositions differ in comparison to the chemical composition of the surface of the electrodes in a coin cell?

The scope of this work only includes investigation of three electrode placements, one where the electrodes are placed 14 mm apart ("stacked" placement), one where the electrodes are side-by-side and one coin cell configuration. The work is also limited to only one set of materials and the scope will therefore not include how different battery systems are effected differently by the electrode placement. The material choices themself, where foil electrodes are used, do also impose limitations since they are bendy. Investigations of the electrode placement in the side-by-side configuration will therefore not be done on electrodes as close together as would be possible with rigid electrodes.

In this thesis, the necessary information about batteries and X-ray Photoelectron Spectroscopy for battery studies will first be introduced in chapters two and three. This will be followed by chapter four, where the studied setups will be described in detail. The experimental method is then presented in chapter five, after which the obtained result and associated discussion will be presented in chapter six. The final chapter of this thesis, chapter seven, will conclude the main findings of this work and discuss the next steps for this project.

Chapter 2

Lithium-Ion Batteries

One type of battery that has become one of the most commonly used after they were first introduce on the market in the early 1990s is the lithium-ion battery (LIB) [5]. They are, for example, used for hand held devices, like phones and laptops, and in electrical vehicles. The development of the LIB has been deemed very important and impactful, which is illustrated by the awarding of the Nobel prize in chemistry in 2019 to John B. Goodenough, M. Stanley Whittingham and Akira Yoshino "for the development of lithium-ion batteries" [6].

LIBs use Li-ions as charge carriers through the electrolyte of the battery. The Li-ions have a charge number of one, meaning that during operation a battery needs to move one ion for every electron that constitute the electrical current used to power a load. Lithium is a very light element and can easily give away electrons, meaning that LIBs have high theoretical specific and gravimetric capacities, as well as a high cell potential [5].

2.1 Battery Operation

Batteries are electrochemical cells that can convert chemical energy to electrical energy [7]. In a battery there are two electrodes with different electrochemical potentials that are separated by an electrolyte, as illustrated in Figure 2.1a. The electrode with higher electrochemical potential is referred to as the positive electrode and the electrode with lower electrochemical potential is referred to as the negative electrode. The terms anode and cathode are also commonly used for the negative and positive electrode, respectively. These terms are however used inconsistently since the anode also refers to an electrode that is oxidized and the cathode to an electrode that is reduced. For a battery, both electrodes are both oxidised and reduced depending on if the battery is being charged or discharged. Due to this inconsistency, the terms anode and cathode will not be used further in this thesis. The electrolyte in between the electrodes is electronically insulating, but still allows a charge to be conducted through the movements of ions. When a battery is being discharged, electrons move from the negative to the positive electrode through an external circuit, while ions move between the electrodes to keep the charge neutrality and close the circuit. A common type of LIB is composed of lithium iron phosphate (LFP) and graphite as the positive and negative electrode, respectively. When the battery is charging, Li-ions leave the LFP, while at the same time, Li-ions in the electrolyte intercalate into the graphite. The opposite happens during discharge, which is illustrated in Figure 2.1b

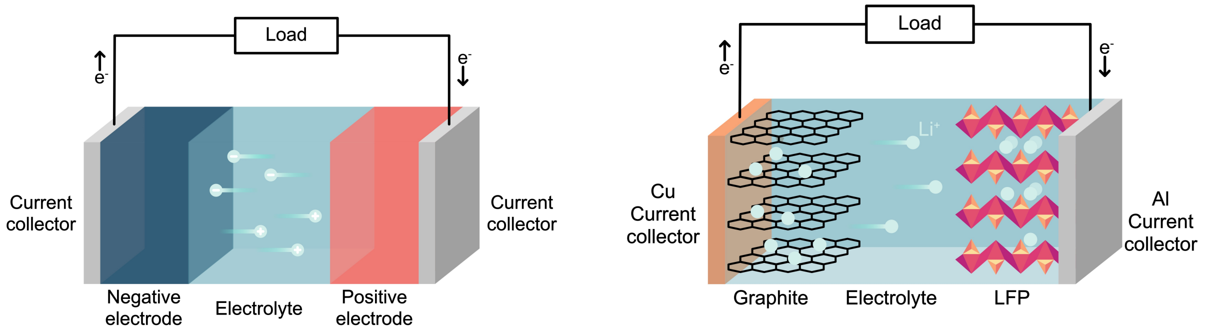

(a) **(b)**

Figure 2.1: a) Working principle and components in a battery. b) Working principle and components in a graphite-LFP LIB.

Even though LIBs are one of the most commonly used type of batteries, they still face serious challenges. Among these, growth of Li on top of the negative electrode, as opposed to intercalation, is one of the main ones [8]. These growths are called dendrites and can lead to varies types of problems. First of all, so called "dead lithium" can form from the dendrites [9]. This lithium is no longer in contact with the negative electrode and can therefore not take part in the redox reaction in the battery. This leads to a loss of capacity. Even more alarming, dendrites can cause a short circuit of the cell [10]. This can in turn lead to thermal runaway and fires. To enable better and safer batteries in the future, understanding the cause of these problems and finding solutions for them is of utmost importance.

2.2 The Solid Electrolyte Interphase

The so-called solid electrolyte interphase (SEI) is a thin layer between the negative electrode and the electrolyte, as depicted schematically in Figure 2.2 [11]. The SEI forms primarily during the first charge cycle due to electrolyte decomposition [12], [13]. The layer is up to tens of nanometers thick and is usually thought to be arranged in a "mosaic" structure with more inorganic species in the inner layer and more organic species near the electrolyte [14]. When formed, a good SEI is insulating to electrons but still allows ions to shuttle between the electrolyte and the negative electrode. This ensures that the battery is still functional after the SEI formation. A similar layer of electrolyte decomposition products is also found on the positive electrode, usually called the cathode electrolyte interphase (CEI), although this layer is observed to be much thinner than the SEI.

The composition of the SEI is of great importance to the performance of LIBs [15]. A good SEI will protect the electrolyte from further decomposition and can even influence, and limit, the dendrite formation. To optimize batteries for safety, high capacity and long cycle life, consideration of the SEI is crucial. Although we know the importance of the SEI, there are aspects to its composition and formation that remain insufficiently understood, especially in its in situ environment [16]. Gaining a deeper understanding of the SEI and the SEI formation will therefore enable the further development of batteries by informing material choices.

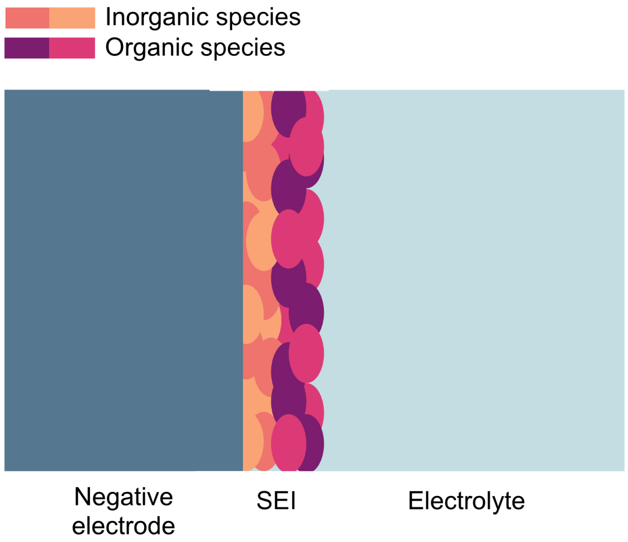

Figure 2.2: Schematic image of the mosaic structure of the SEI.

Chapter 3

X-ray Photoelectron Spectroscopy on Batteries

3.1 X-ray Photoelectron Spectroscopy

In 1921, the Nobel Prize in Physics was awarded to Albert Einstein for his explanation of the photoelectric effect [17]. This effect describes how electrons absorb energy from photons. If the energy of the photon is higher than the binding energy of the electron, it is emitted from the atom. If the absorbed photon has a high energy, like X-rays, even core electrons can be emitted, as is depicted in Figure 3.1a. After the emission of a core electron, the atom relaxes to a lower energy state by having an electron from an outer electron shell fall into the vacancy left by the emitted core electron. The excess energy from the relaxation is either emitted as characteristic X-rays (Figure 3.1b) or transferred to another electron that gets ejected from the atom and is known as an Auger electron (Figure 4.1) [18].

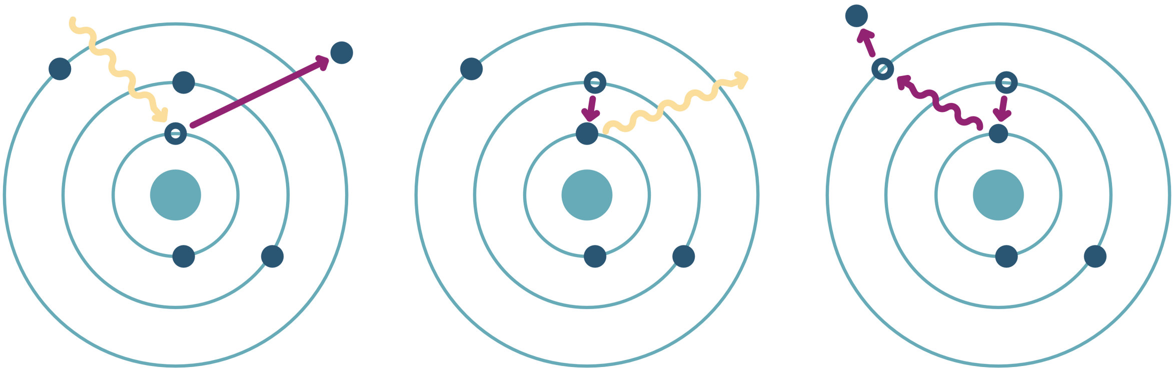
(a) (b) (c)

Figure 3.1: Electron-photon interaction in matter. a) Emission of a core photoelectron. b) Emission of characteristic X-rays during the relaxation after the emission of a core photoelectron. c) Emission of an Auger electron during the relaxation after the emission of a core photoelectron.

The photoelectric effect is used to analyse the surfaces of materials in X-ray photoelectron spectroscopy (XPS). In XPS, X-rays of a known energy are irradiated on the sample surface, resulting in the absorption of photons and emission of core electrons from the sample [19]. By measuring the kinetic energy of the emitted photoelectron, E_{kin}, the binding energy of the electron, E_{B}, can be calculated using

$$E_{\mathrm{B}} = E_{\lambda} - (E_{\mathrm{kin}} + \phi), \tag{3.1}$$

where E_{λ} is the known X-ray energy and ϕ is the known work function of the spectrometer used. The binding energies can then be used to determine the element present on the sample surface.

To measure the kinetic energy of the emitted electrons, a hemispheric analyser is used, which can be seen in Figure 3.2 [19]. When the sample is irradiated, the emitted photoelectrons enter a lens-system where they are retarded and focused towards the entry of the hemispheric analyser [20]. The hemispheric analyser has two concentric hemispheres with different potentials. This creates an electric field within the hemisphere that bends the path of the entering electrons. How much they are bent is determined by their kinetic energy. Only certain trajectories hit the detector which is illustrated in Figure 3.2, where each colour shows the trajectories that reach each photomultiplier that is part of the detector. Electrons with more or less energy will be deflected too much or to little in the the hemisphere to fit on either of those trajectories and can therefore not be detected. This means that only electrons within a certain energy range are detected. This energy range is defined by the pass energy. The pass energy is the energy corresponding to the path with a radius of $(\mathrm{R}_1+\mathrm{R}_2)/2$, where R_1 and R_2 is the radius of the inner and outer wall of the hemispheric analyser [21]. A lower pass energy results in a better energy resolution. This is however accompanied by a lower signal intensity since fewer electrons will hit the detectors.

To decide which energy ranges that are measured, the amount of which the electrons are retarded is altered before the electrons enter the hemispheric analyser. This is done by the electrostatic lenses. The electrostatic lenses shift the kinetic energy of the electrons to the pre-selected pass energy, so together they define what energy range is measured. The pass energy defines the size of the range, while the electrostatic lenses sweep the kinetic energies through that range.

During the XPS measurements, the X-rays penetrate deep into the sample and photoelectrons are subsequently produced throughout the bulk of the sample. However, it is only the photoelectrons produced close to the surface that can escape the sample and be detected. This is a result of the short inelastic mean free path of the electrons in the sample, meaning that the average distance the electron travel before interacting inelastically with the material is short. XPS is therefore a very surface sensitive technique. How surface sensitive depends on the X-ray energy. Higher X-ray energies produce photoelectrons with more kinetic energy, and these have a longer inelastic mean free path compared to photoelectrons with less kinetic energy in the range of energies relevant for XPS. Depending on the X-ray source, the probing depth can therefore vary since it is approximated to be equal to three times the inelastic mean free path [21]. Usually, the probing depth is between 5 and 10 nm [22].

The obtained XPS-spectra show the number of electrons detected with a certain kinetic energy, which gets converted to binding energy by equation 3.1 [19]. This

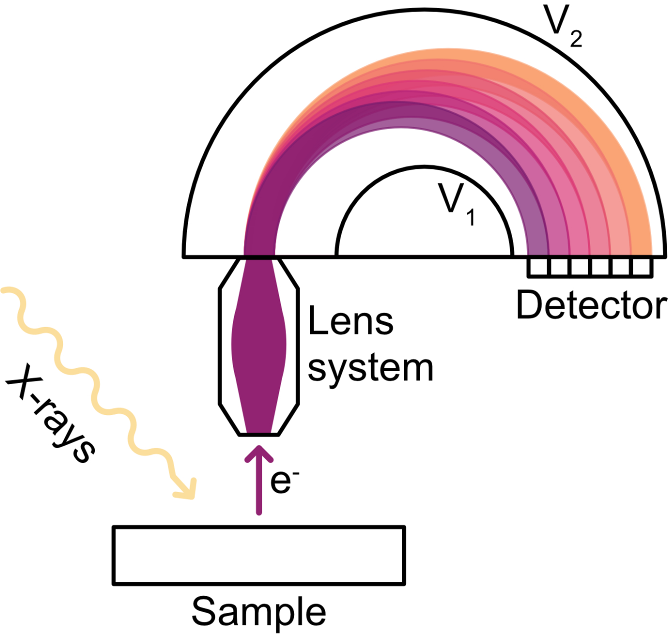

Figure 3.2: Instrument used for XPS measurements.

means that peaks will show at binding energies corresponding to elements present on the surface of the sample. Additionally, in the XPS spectra, different oxidation states will shift the position of the peaks. This change of binding energy comes from the change of effective charge felt by the electron [23]. For example, if a carbon atom is bound to an oxygen or fluorine atom, some negative charge will be moved away from the carbon. The remaining electrons will therefore feel a stronger positive attraction to the atom core, resulting in a higher binding energy. This is what makes it possible to analyse the chemical species, not just the elemental composition, using XPS.

Since the analyser only measures electron kinetic energies, irrespective of the process generating the electrons, Auger electrons will also result in peaks in the spectra. But, as opposed to the photoelectrons, these will be found at a constant kinetic energy instead of constant binding energy for a certain element. This is however not just an unwanted artifact. The Auger peaks will also give useful information about the material. For example, in Cu, the oxidation state can be hard to determine without looking at the shape of the Auger spectra [24]. The spectra will, apart from the photoelectron and Auger peaks, also have a background originating from photo or Auger electrons that have lost their energy in one or multiple scattering events [25]. If the X-ray light is not monochromatic, photoelectrons emitted by bremsstrahlung can also contribute to the background.

3.2 Ambient Pressure XPS

In XPS, the kinetic energy of the electrons emitted from the sample is used to determine the chemical composition and environment of the surface of the sample. For this to work, the electrons need to reach the electron energy analyser without losing any of their kinetic energy. This means that, traditionally, XPS has been performed in ultra-high vacuum (UHV). In UHV, the electrons have a very low likelihood of interacting with remaining gas particles and lose energy on their way to the electron energy analyser. Since the size of the hemispherical analyser is in the order of decimeters, UHV is required in this part of the system, otherwise the measured electrons would all go through scattering events where the relevant information, the binding energies, would be lost. For systems with liquid or gas phase components, the UHV environment is not viable since these components would be pumped away. An alternative technique to UHV XPS can in these instances be used instead: ambient pressure XPS (AP-XPS).

AP-XPS on liquid samples has been possible since the 70's [26], and the technique has since then been refined [27]. The technique relies on differential pumping where the pressure incrementally gets lower in stages as the electron enters the lens system. This allows for the pressure in the sample chamber to reach up to tens of millibars, while keeping the pressure at the electron energy analyser at UHV. To minimize the interaction with particles in the chamber, the sample is usually placed less than 1 mm from the analyser nozzle and higher photon energies can sometimes be utilized to get a larger probing depth that reaches through gaseous vapour.

3.3 Dip-and-Pull Experiments on Batteries

While AP-XPS removes the UHV constraints allowing liquid battery electrolyte to be present in XPS measurements, further compromises need to be considered for performing electrochemical cycling of a battery inside an AP-XPS instrument. In batteries, the positive and negative electrodes are usually pressed together, only separated by a thin separator that makes sure that the electrodes are not in electrical contact. With this electrode configuration, the battery needs to be opened up to perform XPS measurements on the electrode surface. Although these post-mortem studies of batteries can give a lot of insight, so called "dip-and-pull" XPS experiments have been developed to study the electrodes without disassembly [28]. For these experiments the electrodes are usually stacked with a separation of over 1 cm as can be seen in Figure 3.3. The electrode being studied, referred to as the working electrode (WE), faces the XPS analysis nozzle while the counter electrode (CE) faces in the opposite direction. The reference electrode (RE) are then placed in-between the WE and CE. During the experiment, the electrodes are dipped in to the electrolyte. When they are pulled up again, a thin electrolyte meniscus will form on the surface of the electrodes. This meniscus makes it possible to continue the electrochemical operation while also taking XPS measurements.

The measurement protocol of dip-and-pull experiments can be designed differently depending on the purpose of the experiment. Firstly, in situ measurements can be performed. In these experiments, the charging/discharging of the battery takes place with the electrodes in the dipped-down position, fully submerged in the electrolyte. The charging and discharging is then paused and the cell voltage is held constant while the electrodes are pulled up and measurements are performed. The electrodes are then dipped down again to continue the charging/discharging. Another set of protocols can be designed for operando measurements instead. During these measurements the charge/discharge of the battery cell is performed in the pulled-up position at the same

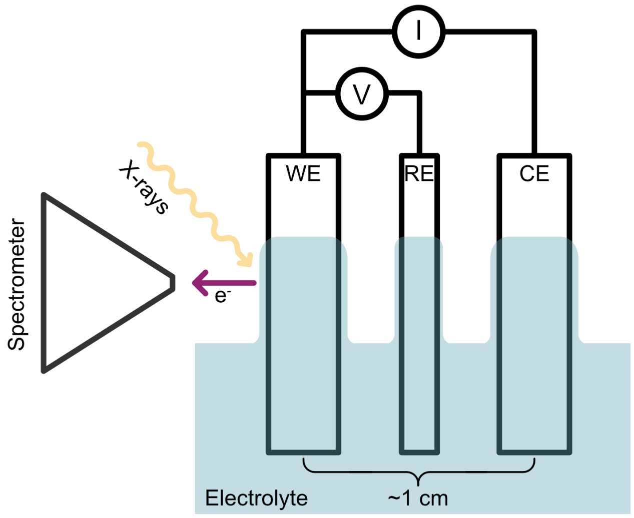

Figure 3.3: Setup for dip-and-pull experiments with working (WE), counter (CE) and reference (RE) electrode.

time as the XPS measurements are performed. For these measurements, dipping of the electrodes is only performed to renew the meniscus. The difference between an in situ and a operando protocol can be seen schematically in Figure 3.4.

Since the thickness of the meniscus does not allow for photoelectrons originating in the electrode to be easily detected when soft and tender X-rays are used, many dip-and-pull studies monitor the potential difference of the interface between the electrode and the meniscus [29]. However, direct probing of the electrodes has recently also been performed [30], [31]. To enable these studies, the so called precursor film is chosen as the measurement area. The precursor film is the area on the very top of the meniscus and it is thin enough that photoelectrons produced from the electrode can be detected, but it still keeps the electrode surface wetted. To be able to probe through the meniscus, tender X-rays are used to ensure the probing depth is large enough for these experiments.

The dip-and-pull experiments are however accompanied by some unwanted artifacts, of which one is the Ohmic drop parallel to the meniscus [32]. A dip-and-pull study in the field of catalysis by Bernadette Davies et al. showed that a factor that could contribute to the observed Ohmic drop is the electrode separation between the electrodes [33]. This study utilized dip-and-pull experiments to investigate the carbon monoxide reduction reaction on Cu(111) with electrodes placed side-by-side, less than 1 mm apart. With this electrode placement, a common aqueous meniscus between the electrodes could be observed. This setup resulted in a reduction of the length charge carriers must be transported compared to the usual, stacked, placement. The study concluded that the changed electrode placement, with a shorter charge carrier path, could limit the Ohmic drop.

The reduction of electrode distance in the side-by-side configuration might also make the

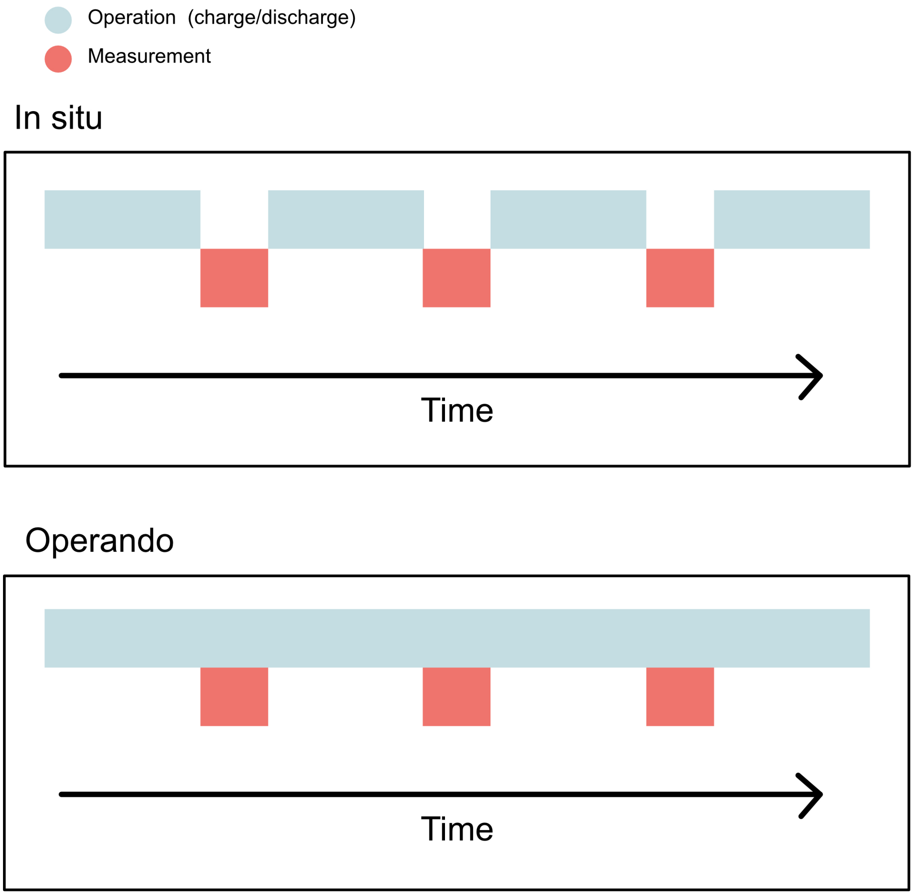

Figure 3.4: Illustration of the procedure of in situ and operando experiments.

dip-and-pull cells more comparable to realistic batteries regarding the SEI composition. A previous study, investigating the effects of electrode distance in coin cells, found that the chemical composition of the SEI on deposited Li does change with electrode distance [34]. For the cell with an electrode distance of 0.5 mm, the composition was similar to the standard coin cell, where the electrodes were only separated with a thin separator (25 μm electrode distance). However, for the cell with an electrode distance of 2 mm, the surface film was thinner and had less C, O and P containing species. This suggests that having an electrode distance of ~0.5 mm could be preferred over larger distances to make conclusions about the composition of the SEI in realistic batteries. However, since the electrodes in a dip-and-pull cell are not facing each other in the side-by-side configuration used by Bernadette Davies et al., these distance effects might not be completely resolved by their proposed setup geometry. Such a geometry has not yet been tested for batteries. To do this is the core topic of this thesis, which can be seen in the following chapters, where the design of a new sample holder is described and the role of electrode placement for operando AP-XPS battery studies is experimentally investigated.

Chapter 4

Experimental Setup and Materials

4.1 Design of Sample Holder

To investigate the role of electrode placement in AP-XPS studies, the sample holder used for these experiments at the HIPPIE beamline at MAX IV was re-designed. The sample holder previously used has the electrodes in a stacked configuration, where the WE and CE separated by 14 mm and facing in opposite direction to allow for AP-XPS measurements as shown in Figure 4.1a.

The re-designed sample holder has to fit on the manipulator at the HIPPIE beamline. This meant that the top part of the sample holder was kept the same, apart from one dimension. The diameter of the hole where the manipulator is attached was made 0.5 mm larger for the re-designed sample holder. This decision was informed by the fit of the stacked sample holder currently in use, where the fit to the manipulator was almost too tight. The bottom part, where the mechanism for electrode attachment is, was changed to facilitate a side-by-side electrode placement (see Figure 4.1b). The side-by-side configuration allows for investigations of both the WE/electrolyte and CE/electrolyte interfaces during the experiments.

Since the electrodes need to be very close to the analyser during the XPS measurements, the decision to clamp the electrodes from the back towards the analyser nozzle was made. This ensures that even if the electrodes are of different thicknesses, the distance to the analyser is the same. This allows for probing of both electrodes by just moving the sample holder in the plane perpendicular to the analyser tip.

The clamp holding the reference electrode is composed of two parts. These parts are clamped together with the reference electrode in-between. The two joint parts can then be attached to the main part of the sample holder. The removability of these parts allows for easier access to the parts that clamp the positive and negative electrode to the main holder.

4.2 Materials

To isolate the role of the electrode placement, commercial materials are used for all experiments. The standardization and reliability of the commercial materials ensure the

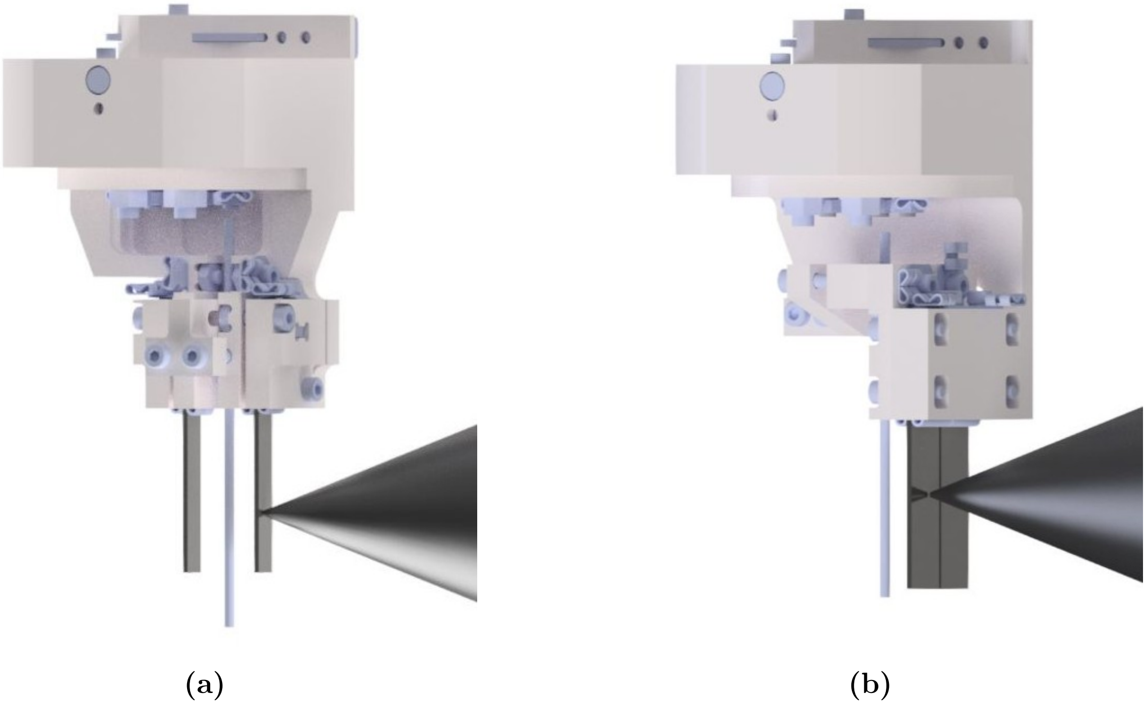
(a) (b)

Figure 4.1: Setups used for dip-and-pull AP-XPS experiments. a) Previous design with a stacked configuration where the electrodes are placed 14 mm apart. b) New design where the electrodes are placed side-by-side, 0.65 mm apart.

comparability between different cells. For the electrodes, coated foils were chosen to enable the same materials to be used in both the beaker cells and in the coin cells.

For the positive electrode, Al foil coated with lithium iron phosphate (LFP), $LiFeO_4$, from Customcells® were used (product item no. 13123, batch K - 1482). This electrode had a reported area capacity of 2 mAh/cm^2. For the negative electrode, Cu foil coated with graphite from Customcells® were used (product item no. 100000020). This electrode had a reported area capacity of 2.4 mAh/cm^2. The electrolyte used was 1 M $LiPF_6$ in ethylene carbonate/diethyl carbonate = 50/50 (v/v) from Sigma-Aldrich.

4.3 In-house Experimental Setup

4.3.1 Beaker Cells

To allow investigating the role of electrode placement, simplified laboratory sample holders that gave the same electrode placement as in the two sample holders designed for HIPPIE beamline were designed. These sample holders were made to stand on their own inside a glovebox as shown in Figure 4.2a and 4.2b. As part of the holder, a stabilizer for the electrolyte beaker (10 ml glass beaker) was also designed to minimize the risk of accidentally tipping the beaker. The stabilizer can be seen in Figure 4.2c. The in-house sample holders were 3D printed in PLA with 100% infill to minimize the risk of trapped air that could contaminate the argon filled glovebox.

For the electrode preparation, the foils were first cut in to strips (0.8 x 5 cm), where only

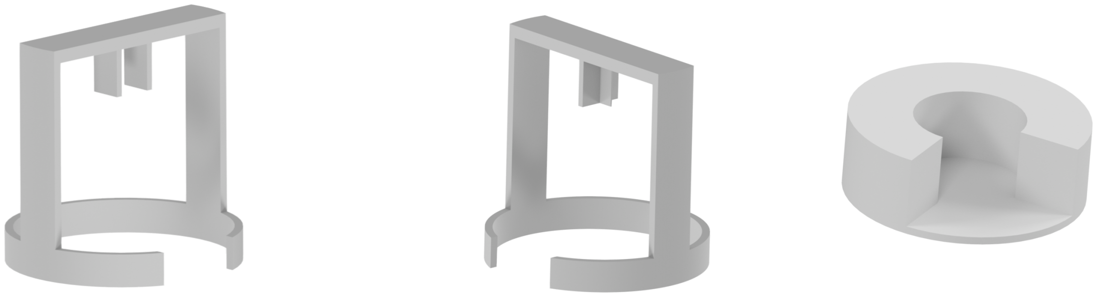
(a) (b) (c)

Figure 4.2: Set ups used for in-house experiments. a) Sample holder with a stacked configuration where the electrodes are placed 14 mm apart. b) Sample holder where the electrodes are placed side-by-side, ∼0.65 mm apart. c) Stabilizer for the electrolyte beaker.

about 2/3 of it was covered with active material. The uncovered part made sure that there was access to the current collector (the foil) from the front of the electrode. The electrodes were then dried in vacuum at 110°C.

During the assembly of the cells, the foil electrodes were placed on top of Al rods (0.8 x 5 cm) that worked as mechanical support to keep the foils in the right position. The electrodes and Al rods were placed on the sample holder, and all parts were clamped together using crocodile clamps. Due to the weight of the cables connected to the potentiostat, connecting wires were used to bridge the gap between them and the crocodile clamps on the sample holder. The electrolyte beaker and stabilizer were put on a spacer (12 mm) that made the electrodes reach almost all the way to the bottom of the beaker. When the electrodes were put in place inside the beaker, 7 ml of electrolyte was added, submerging 1.36 ±0.1 cm^2 of the electrodes. This mimics the dipped down position for the electrodes in a dip-and-pull experiment. A large beaker (1800 ml) was lastly put on top of the sample holder to limit electrolyte evaporation inside the glovebox. The setup can be seen in Figure 4.3.

4.3.2 Coin Cells

The coin cell electrodes were punched into circles with a diameter of 13mm and dried in vacuum at 110°C overnight. The coin cells were then assembled using 100 μl electrolyte and a glass fiber separator (Whatman). The coin cell components can be seen in Figure 4.4

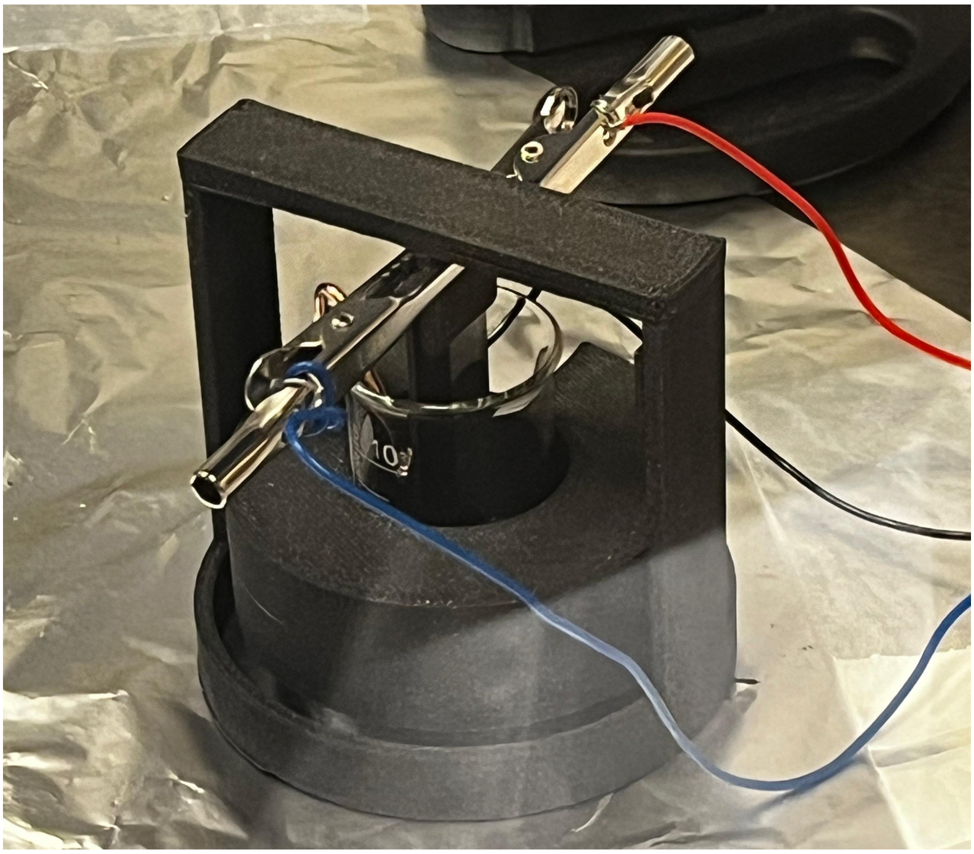

Figure 4.3: In-house beaker cell setup inside of a glovebox.

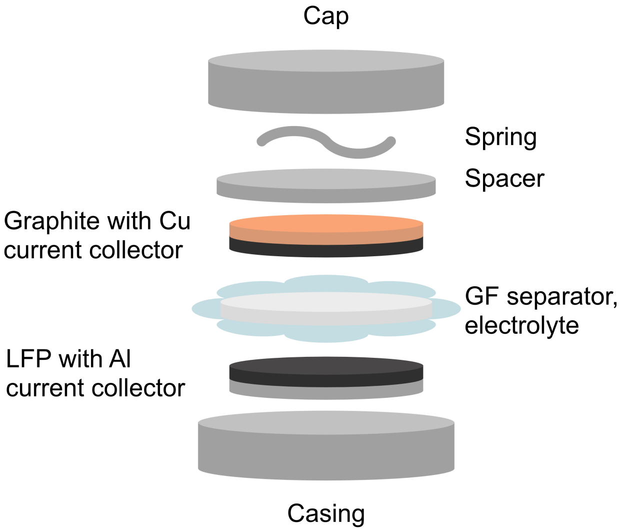

Figure 4.4: Components of a coin cell. During assembly, all parts are pressed together and sealed with a hydraulic crimper.

Chapter 5

Experimental Methods

To investigate how the electrochemical performance, resistances and surface composition of a battery are affected by the electrode placement, three experimental methods were used: galvanostatic cycling, electrochemical impedance spectroscopy and X-ray photoelectron spectroscopy. In this chapter, these techniques will be introduced and the experimental procedures will be described in detail.

5.1 Galvanostatic Cycling

During galvanostatic cycling, the battery is being charged and discharged with a constant current. The current is usually set to get a specific C-rate, meaning how many times the battery can be fully charged or discharged in one hour given the theoretical capacity. The cycles are often limited by an upper and a lower cut-off voltage that are set based on the material properties. By monitoring how the cell voltage changes with the total charge transfer over time, the practical capacity and capacity degradation of the system can be studied. This allows for investigation of the cell performance.

For this thesis project, one cycle of galvanostatic cycling was performed at a C-rate of about C/10 for all three cell setups. For the cycling, three different potentiostats were used: a Gamry reference 600, a Scribner 580 battery test system and a Biologic VMP-3. The lower and higher potential limits were 2.5 and 4 V, respectively. The area of the electrodes submerged in the electrolyte was 1.36 ± 0.1 cm^2 for the in-plane and stacked beaker cells, and $\sim$1.33 cm^2 for the coin cells. The uncertainty in area for the beaker cells is calculated from an estimate of how accurately the electrode could be placed. However, more uncertainties are most likely present since non-submerged parts of the electrodes are probably soaking up electrolyte and therefore contributing to the total capacity. How much this contributes is however hard to determine, which needs to be taken into consideration when analysing the data. Given the areal capacity of the LFP electrode (2 mAh/cm^2), the currents used for the experiment were 0.272 and 0.265 mA. For the stacked electrode configuration, the cycling was performed at 0.265 mA instead of 0.272 by mistake. This resulted in a C-rate of 10.264 instead of 10. The discrepancy in C-rate is however thought to be so small that it does not impact the conclusions that can be drawn from the results.

5.2 Electrochemical Impedance Spectroscopy

Electrochemical impedance spectroscopy (EIS) is a common technique used to study the impedance of a system [35]. During (potentiostatic) EIS, the current response of a varying voltage input is observed as a function of the voltage frequency [36]. The obtained result is usually displayed in a Nyquist plot, where the imaginary part of the impedance is plotted against the real part. The resulting plot is usually comprised of one or multiple semicircles. The size and position of the semicircles are related to the impedance of the system. For a simple system, showing only one semicircle as in Figure 5.1b, the equivalent system can be represented by the parallel coupling of a resistance and a capacitance in series with a resistance as in Figure 5.1b. In this simplified system, the R_1 resistance is usually related to the electrolyte, while the R_2 resistance is related to the charge transfer.

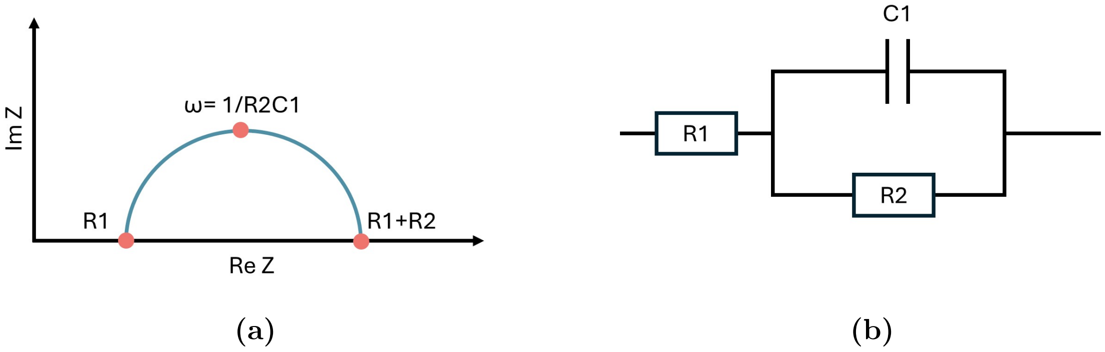

(a) (b)

Figure 5.1: The EIS behaviour (a) of the corresponding equivalent circuit (b).

For this work, EIS was performed with a Biologic potentiostat for the coin cell and a Gamry reference 600 for the beaker cells. The electrodes were left at OCV for 4 hours before measurement. The measurements were done at frequencies between 1 M Hz and 100 mHz in steps of 10 points per decade and 5 measures per frequency. The applied potential was sinusoidal around the OCV with an amplitude of 10 mV.

5.3 X-ray Photoelectron Spectroscopy

To study the chemical composition of the electrode surfaces, post-mortem XPS was performed on the positive and negative electrodes for the three cell setups. Before measurement, the electrodes were cycled using the galvanostatic cycling protocol described in section 5.1. For the two in-house beaker cell setups, ~3x8 mm^2 pieces of the LFP and graphite foils were cut off and washed in 2 ml of dimethyl carbonate (DMC) by submerging and stirring the foils for 1 minute. The foils were then attached to the XPS-sample holder using conductive copper tape. The coin cell electrodes were also cut into ~3x8 mm^2 pieces, after which they were rinsed with 1 ml DMC and attached to the XPS-mount using copper tape. Pristine LFP and graphite foils were also cut and attached in the same way, but without any washing. These were then used as references for the cycled material. The electrode pieces were left to dry in the argon filled glovebox and then transferred to the XPS analysis chamber using an air-tight transfer vessel to make sure they were kept under inert conditions during the entire transfer process. After the transfer, the load lock was pumped overnight before the sample was introduced to the analysis chamber

For the XPS measurements, a PHI Versaprobe III XPS was used with a Al K_α X-ray source (monochromatic, 1486.6 eV). Spectra were acquired for the F 1s, C 1s, O 1s, P 2p and Li 1s core levels for the graphite and the F 1s, C 1s, O 1s, P 2p, Li 1s and Fe 2p core levels for the LFP. The pass energy for these measurements was 55 eV. A survey spectrum was also acquired with a pass energy of 224 eV for all samples to detect potential contaminants. For all measurements the step size was 0.1 eV with a time of 20 ms per step, the X-ray power was 50 W and the X-ray spot was 200 μm. Binding energy calibration and referencing was not altered for the system.

Chapter 6

Results and Discussion

This chapter presents the result of the experiments performed during this project. The results are also analysed and discussed to answer the formulated research questions of how the electrode placement affects the electrochemical performance and resistances of the cells as well as the surface composition of the electrodes.

6.1 Galvanostatic Cycling

Galvanostatic cycling allows to compare the capacities as well as the charge and discharge potential curves for the different cells. The capacity performance of all studied cells can be seen in Figure 6.1. The two beaker cells perform somewhat similar while the coin cells have a larger capacity, both regarding charge capacity in relation to theoretical capacity and discharge capacity in relation to the charge capacity. It can also be noticed that the coin cell performance varies less between different cells since all four of the data points from the coin cells overlap.

The discharge capacities of the coin cells are at over 80% of the charge capacity, while the beaker cells have only retained about half of the charge capacity for the discharge. All cells have a lower discharge capacity compared to charge capacity in the first cycle. This is, to some degree, expected to be a result of the SEI formation [37]. However, the degree of capacity loss in the beaker cells indicates additional irreversible reactions.

The voltage curves for one cell of each configuration can be seen in Figure 6.2. All measured voltage curves can also be seen in Figure A.1-A.3. The shape of the potential curves during the charge and discharge looks similar between the two beaker cells, but differs in some ways compared to the coin cell. One noticeable difference is that there is a voltage peak before the longer plateau during the charge cycle (at about 2 hours of charging) for the beaker cells that is not present for the coin cell. This peak could be related to the nucleation of a new phase in the beaker cell electrodes, more specifically to a high activation energy for the phase nucleation of the transition $LiFePO_4 \rightarrow FePO_4$ [38], [39], [40]. Since this peak is not present for the coin cell, the nucleation of $FePO_4$ does not seem to require as much activation energy in these cells. The difference in transition pathway due to the higher activation energy in the beaker cell can potentially cause irreversible reactions [41]. This could therefore contribute to the low discharge capacity observed in the beaker cells.

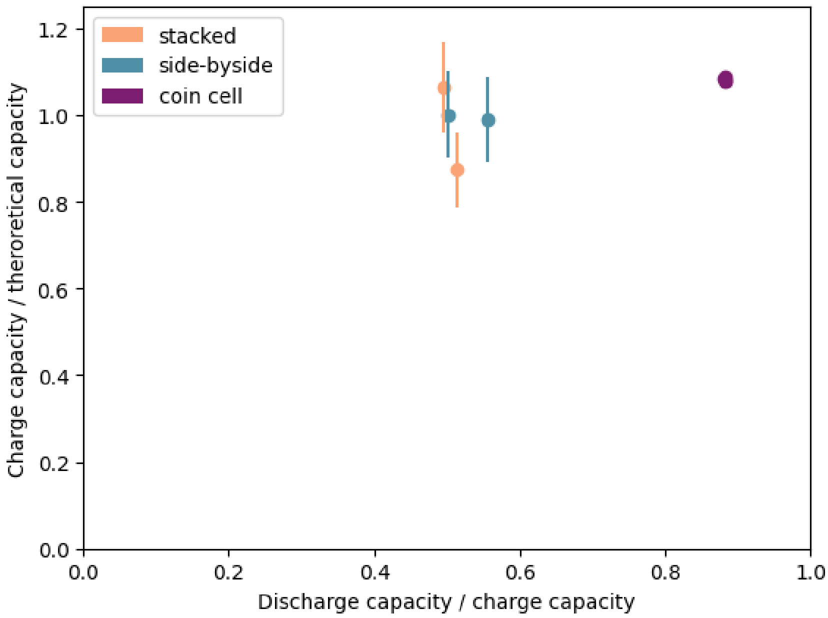

Figure 6.1: Comparison of the discharge capacity in relation to charge capacity and the charge capacity in relation to theoretical capacity for the coin cell, side-by-side and stacked electrode placement. Error bars are calculated from the uncertainty of the wetted electrode area for the beaker cells (±0.1 cm^2). Further uncertainties could be present since the porous materials used could soak up electrolyte even in the parts that are not submerged in the electrolyte. Notice that the data of the four coin cells are so similar that their data points overlap.

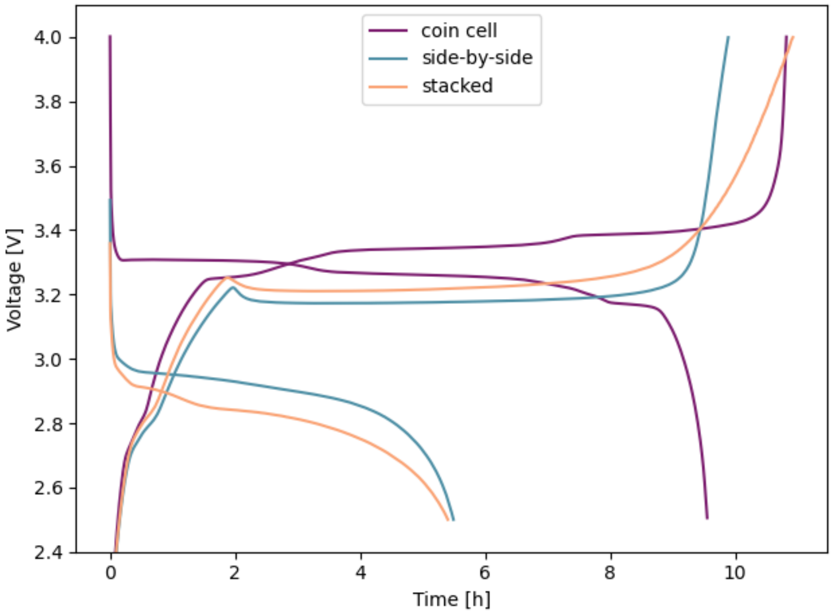

Figure 6.2: Voltage curve during charge and discharge for the coin cell, side-by-side and stacked electrode placement with a C-rate of ~C/10. The charging curves start in the bottom left and end in the upper right corner, while the discharge curves start in the upper left and end in the lower right corner.

Another difference between the voltage curves is the number of plateaus present for the coin cell and beaker cells. For the coin cell, multiple distinct plateaus can be observed, matching well with previous studies on intercalation/deintercalation of Li-ions in graphite [42]. For the beaker cells, there is only one plateau. This could mean that other reactions make the distinct plateaus less noticeable. It could also be that we only have one plateau and that a large over-potential is seen when the next plateau is reached that makes the voltage reach the cut-off voltage at 4 V. In this case, the first plateau is over 6 hours, which means that the electrolyte must have wetted more of the porous electrodes to enable a higher theoretical capacity than what was assumed by calculating the submerged area. The differences observed could indicate that the electrochemical performance is affected by the electrode placement. Since the differences are mainly observed between the two beaker cells and the coin cell, other aspects, such as the open beaker cell or the difference in electrolyte volume, could however also give rise to the differences in electrochemical performance.

6.2 Electrochemical Impedance Spectroscopy

To investigate the role of electrode placement for the resistances in the different cells, EIS has been performed in the frequency range between 1 MHz 100 mHz after 4 hours of OCV. The EIS shows one semicircle followed by a tail for all cells, which can be seen in Figure 6.3. The EIS can also be viewed individually for each cell in Figure A.4-A.6. It can be noticed that the semicircle grows in size and moves to the right when the distance between electrodes gets bigger. This indicate that the resistances are biggest in the stacked configuration and smallest in the coin cell configuration. This could be further supported by fitting the data to an $R_1 + C_1/R_2$ equivalent circuit, as seen in Figure 5.1b, coupled in series with a diffusion or Warburg component, W. The obtained parameters from the fitting can be seen in Table 6.1.

The results show that both the resistance related to the electrolyte (R_1) and the resistance related to the charge transfer (R_2) are significantly lower for the coin cell compared to the beaker cells. Furthermore, between the beaker cells, the side-by-side configuration shows lower resistances. The stacked configuration has more than twice the resistance for R_1 and more than four times the resistance for R_2 compared to the side-by-side configuration.

The results indicate that the electrode placement does affect the resistances of battery cells. The low resistance of the coin cell could be a result of the small distance between the electrodes, but also an effect of the pressure on the cell from the spring and casing. Between the two beaker cells, the difference in the distance between the electrodes is likely what causes the difference in resistances. However, this work has been performed with a two-electrode setup where the negative electrode works as both counter and reference electrode. This effectively means that the EIS has been performed with different reference electrode placements in the different setups. Since the placement of the reference electrode itself can influence the EIS, the difference in the reference setup can have altered the EIS result [43]. To validate the result obtained in this work, EIS should therefore be performed with a reference electrode placed close to the negative electrode for the beaker cells.

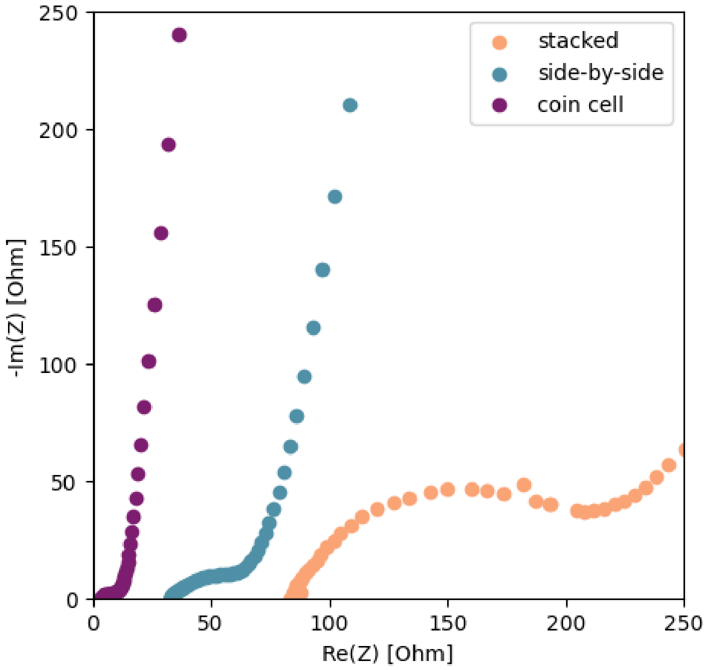

Figure 6.3: Nyquist plot of the EIS data for the coin cell and the beaker cells.

Table 6.1: Resistances and capacitance obtained by fitting the EIS data to an $R_1 + C_1/R_2 + W$ equivalent circuit for the stacked, side-by-side and coin cell configuration.

	R_1 [Ohm]	R_2 [Ohm]	C_1 [F]
Stacked	84.42	114.1	$5.241 \cdot 10^{-6}$
Side-by-side	32.5	28.31	$20.65 \cdot 10^{-6}$
Coin cell	4.392	2.98	$13.32 \cdot 10^{-6}$

6.3 X-ray Photoelectron Spectroscopy

To investigate how the cycling impacted the surface composition on the electrodes, XPS was performed on both the positive and negative electrode in all cell configurations. Additionally, XPS measurements were also performed on pristine graphite and LFP.

Survey spectra for the graphite samples are found in Figure 6.4 for all electrode configurations as well as for a pristine electrode. From the survey, we can see that all cycled cells show the same peaks at about 688, 530, 285, 138 and 57 eV, corresponding to the presence of F, O, C, P and Li on all samples. However, the relative peak intensities vary between samples, meaning that the elemental concentrations differ.

The elemental concentrations were calculated from the survey spectra as well as the relative sensitivity factors given in Table A.1. The concentrations are presented in Figure 6.5. For pristine graphite, most of the signal comes from carbon which is expected since the graphite itself is made up of carbon. Oxygen is also present on the surface. The oxygen can come from the binder, although this can not be confirmed since the manufacturer does not disclose the binder used in the data sheet. The oxygen can also indicate that some contamination is present. Adventitious carbon species, which include some oxygen, are a known problem for studies on surfaces [44]. This is because they are

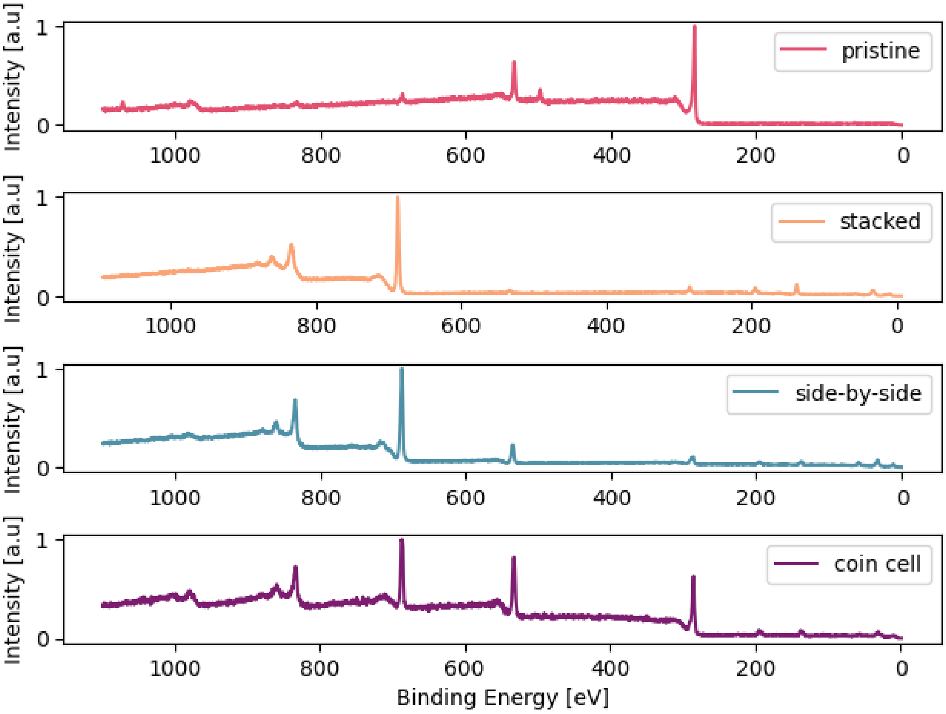

Figure 6.4: Survey spectra for pristine graphite as well as graphite cycled in the stacked, side-by-side and coin cell configuration.

so common that they are hard to avoid. Because of this, they are a probable source of the detected oxygen. This indicates that some of the carbon intensity is likely also due to contamination. For the pristine graphite, small amounts of fluorine and phosphorus are also found. These contaminations are, as opposed to the oxygen contamination, not expected. The cause of it is likely environmental contamination from either the glovebox in which the electrodes were mounted on the XPS sample holder or the XPS analysis chamber itself.

For the cycled electrodes in the stacked, side-by-side and coin cell configurations, the surface composition changes compared to the pristine graphite electrode. It can be observed that the stacked and side-by-side configurations result in a surface composition similar to each other. They both have large amounts of fluorine and lithium and only ∼10% (atomic percentage) carbon and oxygen. For the coin cell, on the other hand, carbon and oxygen make up over 40% and 20% of the total composition, respectively. At the same time, the coin cell graphite electrode has significantly less fluorine and lithium. This indicates that the graphite surface in the coin cell has much more organic species in the formed SEI, while the beaker cells have an SEI with more inorganic species containing lithium and fluorine. Another explanation for the excess fluorine and lithium could be that it is from electrolyte salts that could not be removed during the washing procedure. Phosphorus is not present in large amounts on any of the samples, but shows the largest presence on the stacked beaker cell electrode.

For the LFP, the survey spectra can be seen in Figure 6.6. Here, peaks can be found at about 710, 686, 285, 531, 136 and 56 eV, corresponding to the presence of Fe, F, O, C, P and Li on the electrode surfaces. The different peaks show about the same relative intensity for all cycled samples, indicating that the elemental concentrations are

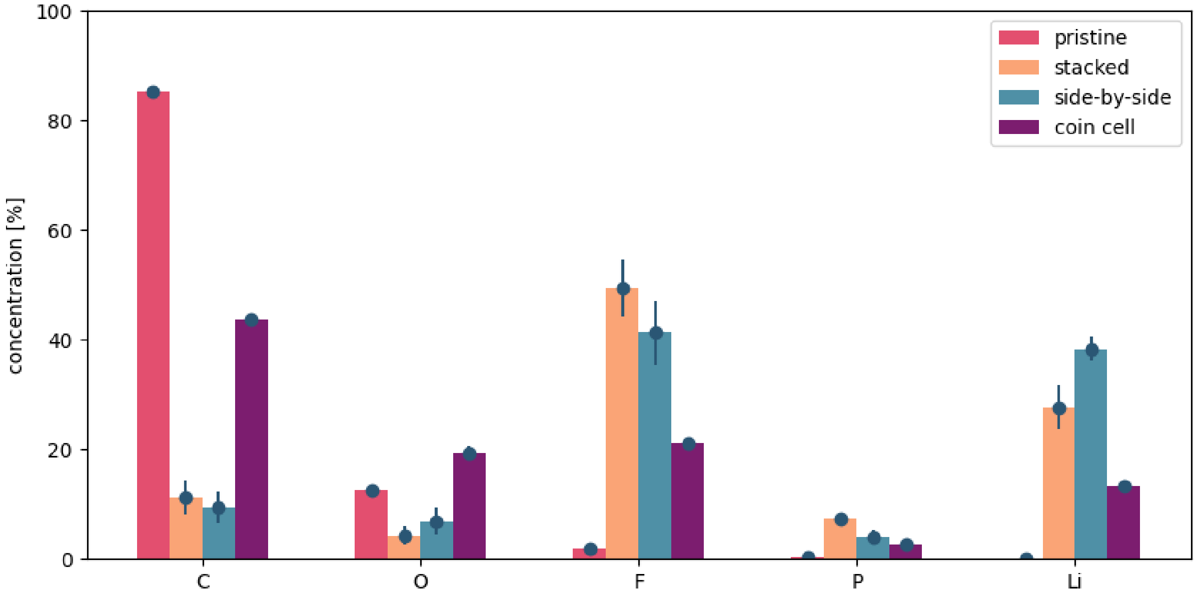

Figure 6.5: Mean atomic concentration of graphite for the stacked and side-by-side beaker cell configurations, as well as for the coin cell configuration and pristine graphite. Error bars show the standard deviation from measurements on different spots on the sample.

about the same on all samples after cycling. The indication of small differences in the elemental concentration between the cycled cells is further supported by Figure 6.7. The differences between the different samples are smaller compared to the graphite samples. As with the graphite, higher concentrations of fluorine can be observed for the beaker cell configurations, but the difference is considerably lower. For the lithium, it is instead the coin cell configuration that shows a slightly higher concentration. The compositions of the cycled electrodes are also similar to the pristine LFP. This indicates that the surface composition of the LFP does not change as much during cycling, compared to the graphite.

The LFP electrodes are made out of $LiPFeO_4$, which stoichiometrically means that the concentration of Li, P and Fe should be the same, while the concentration of O should be about four times higher than the other elements on pristine LFP. This fits with the measured concentrations of the F, Fe and O. However, the Li concentration is almost ten times higher than expected. The reason for this is unknown, but a possible explanation is that the Li is present to a greater extent on the surface compared to the bulk. A significant carbon concentration is expected since carbon is included in the binder and conductive carbon additive for the LFP electrodes [45]. However, similar to the graphite, some of the carbon signal probably originates from contamination as well.

For further evaluation, detailed spectra of the C 1s, F 1s and P 2p core levels were fitted. For the graphite spectra, seen in Figure 6.8, we find a peak in the C 1s spectrum for pristine graphite at 284.5 eV, corresponding to graphitic carbon (sp^2). We can also see a peak at 285 eV for saturated hydrocarbons (sp^3). At even higher binding energies (286, 289, 290 and 292 eV) we find evidence indicating increasingly higher oxygen coordinated carbon, further supporting the existence of some contamination on the samples. The binding energies of the peaks in F 1s (687 eV) and P 2p (doublet at 137 eV) match

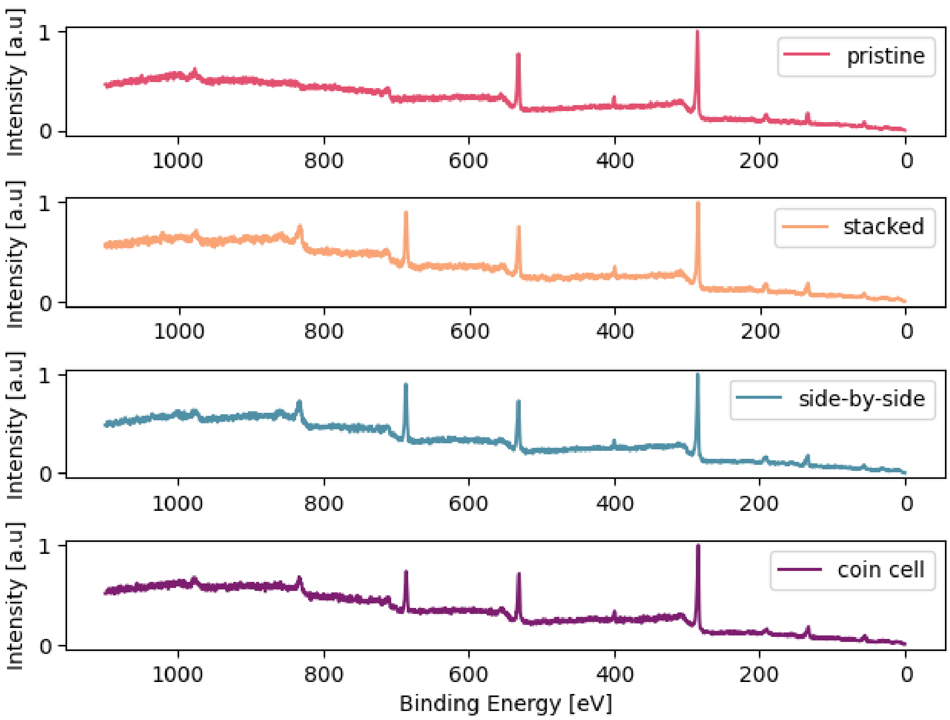

Figure 6.6: Survey spectra for pristine LFP as well as LFP cycled in the stacked, side-by-side and coin cell configuration.

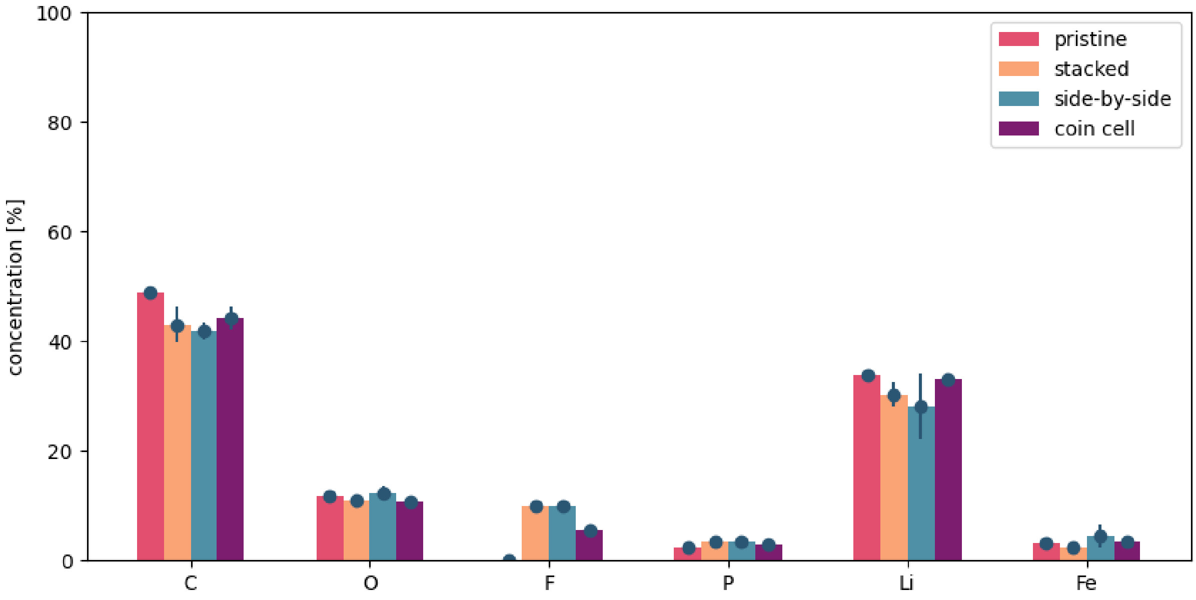

Figure 6.7: Mean atomic concentration of LFP for the stacked and side-by-side beaker cell configurations, as well as for the coin cell configuration and pristine LFP. Error bars show the standard deviation from measurements on different spots on the sample.

$LiPF_6$ decomposition products, confirming that these species come from glove box contaminations

For the cycled electrodes, we can see that the graphite peak in the C 1s spectra at about 284.5 eV decreases for the coin cell configuration and disappears almost completely for

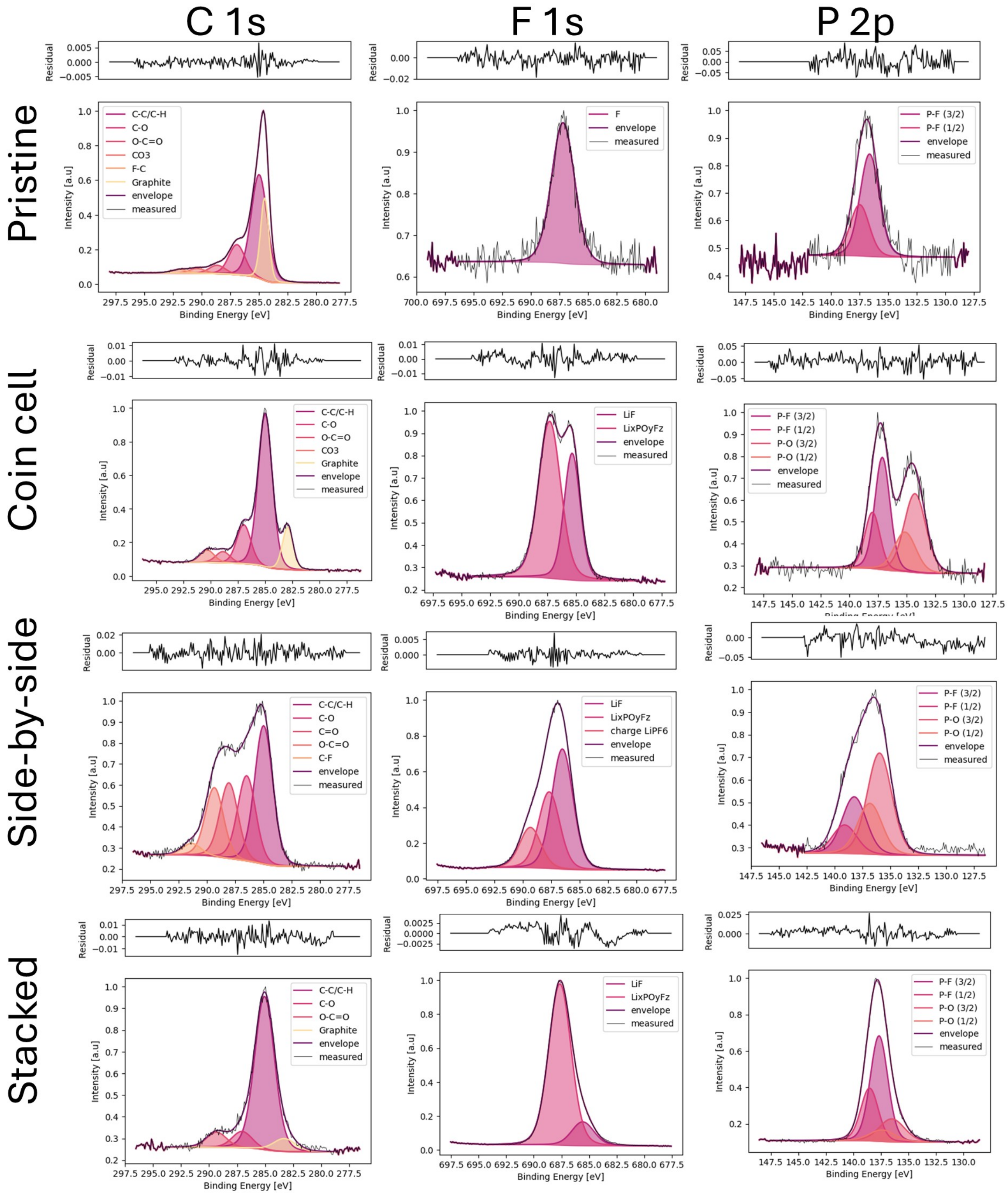

Figure 6.8: Fitted spectra for the C 1s, F 1s and P 2p core level for pristine graphite as well as cycled graphite in the coin cell, side-by-side and stacked configuration. The coin cell, side-by-side and stacked spectra were calibrated to have the C-C/C-H peak at 285 eV. For the pristine spectrum, no calibration was needed.

the two beaker cell configurations. The larger decrease for the beaker cells indicates that the photoelectrons cannot get through the SEI/surface layer for the beaker cell electrodes, meaning that we probably have a thicker SEI/surface layer on these electrodes compared to the coin cell electrode. Furthermore, even though the concentration of carbon is similar between the electrodes cycled in the two beaker cells, it can be noticed from the fitting that the C 1s spectrum looks different. The side-by-side configuration has more species with higher binding energies, possibly corresponding to oxidized carbon (288, 290 and 291 eV) and species with C-F bonds (293 eV). The stacked configuration, on the other hand, has more signal from the peak at 285 eV, corresponding to saturated hydrocarbons. This could indicate differences in the surface composition. However, another possible explanation is that the high energy signals from the side-by-side configuration originates from charging of the sample.

For the F 1s and P 2p peaks on the cycled graphite electrodes, the fittings show slight variations as well. For the coin cell electrode, the two distinct peaks are seen for the F 1s core level at 685 and 687 eV, assigned to LiF and oxygenated salt decomposition product ($Li_xPO_yF_z$), respectively. The two doublet peaks at about 137.5 and 135.5 eV for the P 2p core level, corresponding to bonding environments in the $Li_xPO_yF_z$, are also distinct peaks.

For the stacked cell, the positions of the F 1s peaks are about the same as for the coin cell, the LiF peak is however much smaller in comparison to the $Li_xPO_yF_z$ peak. The two peaks in the spectra are therefore no longer separated. The doublet peaks for the P 2p core level have both moved to higher energies (137 and 138 eV, respectively) and the ratio of the P-O peak is smaller than the P-F peak in comparison to the coin cell. Since the binding energies are closer together compared with the coin cell, the two peaks are not separated here either. For the side-by-side cell, a third peak emerges at about 688.5 eV for the F 1s core level in comparison to the coin and stacked cell. The high energy suggests that this is caused by charging. This is consistent with the P 2p core level, where the P-F doublet peaks are at higher energies (139 eV) compared to the other cells. The P-O doublet peak is still at about 136 eV, which is about the same as for the other cells. This suggests that the charging affects a phosphorous and fluorine containing specie. A likely candidate is $LiPF_6$.

For the side-by-side configuration, different spots also gave different spectra. The spectra of the F 1s and P 2p core levels for two different spots on the same sample can be seen in Figure 6.9. The peak at about 691 eV (688 eV peak with calibration) is significantly larger in spot 2 for the F 1s core level. A high energy peak at 141 eV is also accompanying this large peak in spot 2, which is seen in the P 2p spectrum. This indicates that there is electronically isolated $LiPF_6$ present on the surface and that this $LiPF_6$ is unevenly distributed. This can explain why the concentration of Li and F is higher for the side-by-side beaker cell compared to the coin cell. However, this does not explain this phenomenon completely since the stacked cell also has a high concentration of Li and F while simultaneously not showing clear signs of charged $LiPF_6$. One explanation could be that the main peak, now labelled as $Li_xPO_yF_z$, for the stacked cell originates from $LiPF_6$ that does not experience charging.

The reason why charging was observed is not known. The graphite electrodes used for this work were however observed to be very fragile and flaky and it is therefore possible that parts of the electrode detached and became electronically isolated post cycling. It is also possible that certain insulating species create parts that are electronically isolated. To further evaluate this, re-doing the measurements on a graphite electrode cycled in the side-by-side configuration could be done. This could also verify that the charging only affects the dried $LiPF_6$ and not other parts, like the organic species. This is important

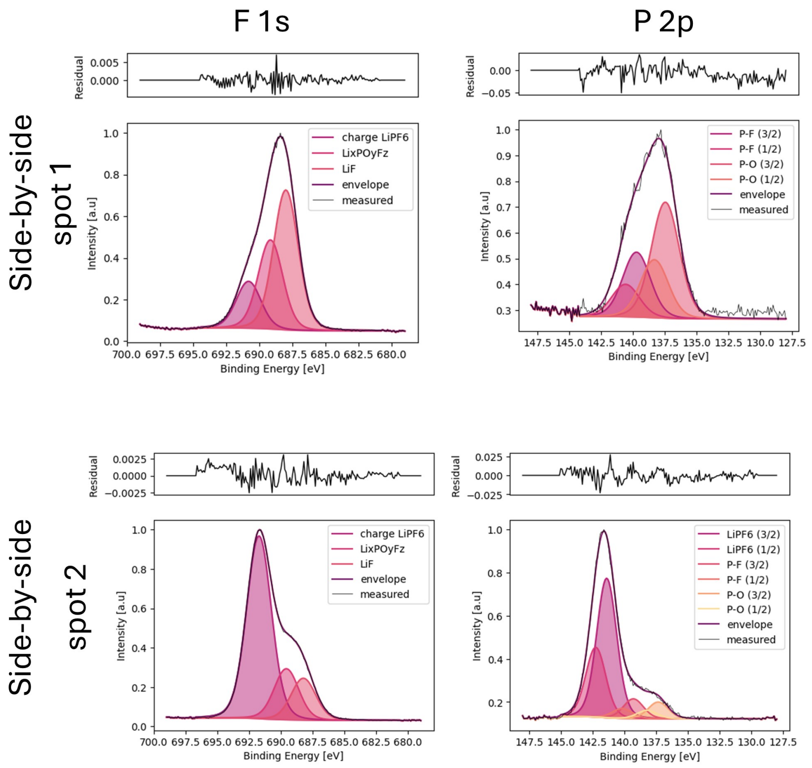

Figure 6.9: Fitted spectra for the F 1s and P 2p core level for two different spots on the same graphite electrode cycled in the side-by-side configuration. The spectra are shown without calibration of the binding energies.

since the C 1s spectrum of the side-by-side electrode looks different compared to the coin cell and stacked cell, indicating that different species form with this configuration if charging does not impact them.

The spectra and fits of the measurements on LFP electrodes can be seen in Figure 6.10. For the C 1s core level, the spectra of the cycled LFP look very similar to the spectrum of pristine LFP. At 284.5 eV, a peak corresponding to sp^2 carbon is seen, probably originating from the conductive additives of the electrode. At higher energies (285, 287 and 289 eV), saturated hydrocarbons and oxidised carbons are also found.

For the pristine LFP electrode, some differences can be seen for the F 1s and P 2p core levels compared to the cycled electrodes. Only one doublet peak can be found on the LFP electrode for the P 2p core level, located at 134 eV. This peak corresponds to $LiFePO_4$. For the F 1s core level, the signal is too small to distinguish from the noise. After cycling, a second doublet peak appears at 136.5 eV alongside the $LiFePO_4$ peak for the P 2p core level. This peak is attributed to a P-F bond, which agrees with the emerging peak at 686 eV in the F 1s spectra. The three different cell configurations for the cycle cells look similar for all core levels, indicating that the electrode placement does not affect the surface composition of the LFP.

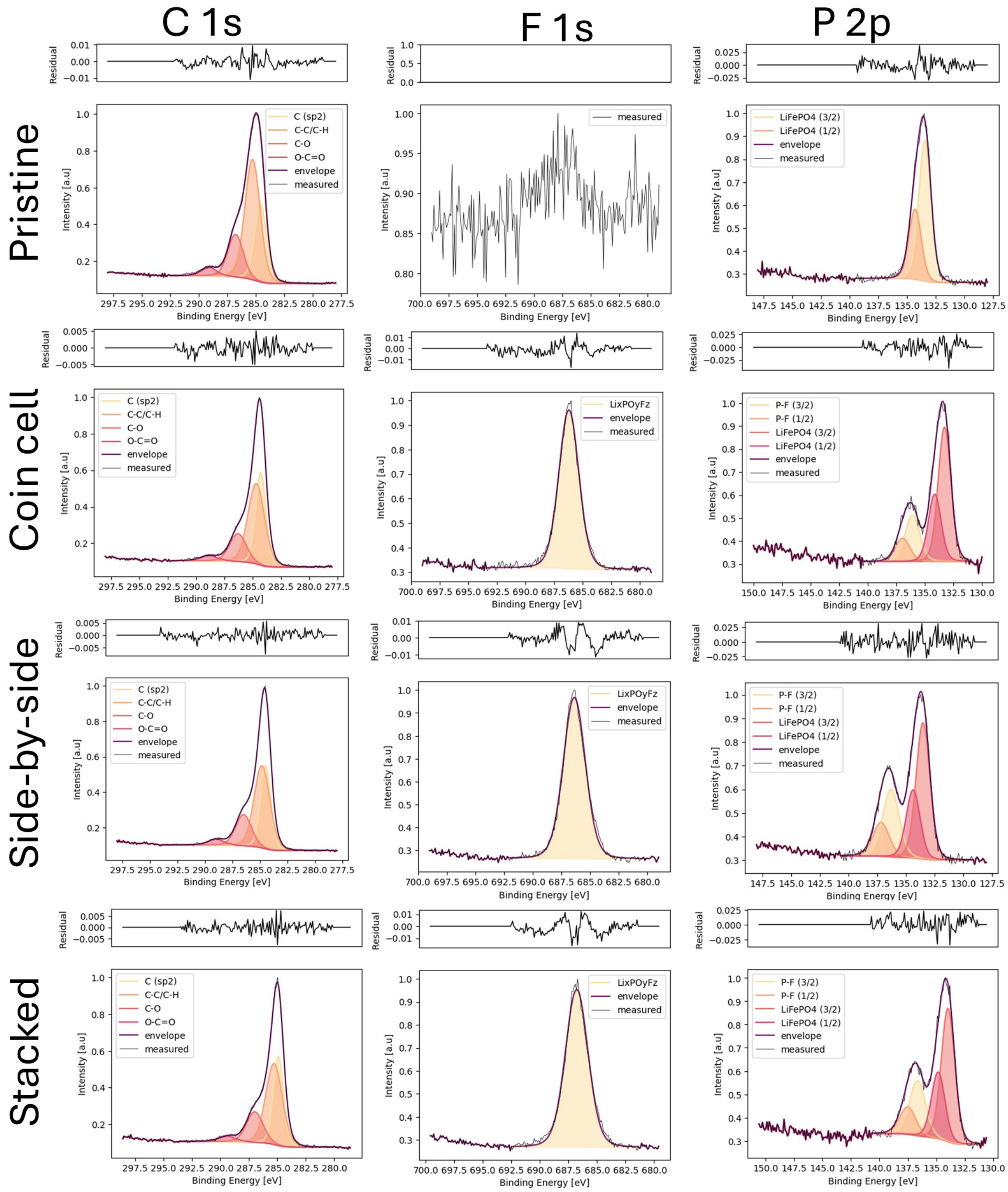

Figure 6.10: Fitted spectra for the C 1s, F 1s and P 2p core level for pristine LFP as well as cycled LFP in the coin cell, side-by-side and stacked configuration. The coin stacked spectra was calibrated to have the C-C/C-H peak at 285 eV. For the pristine coin cell and side-by-side spectra, no calibration was needed.

In conclusion, graphite electrodes show higher concentrations of lithium and fluorine on the surface if they are cycled in beaker cells compared to coin cells. The signal of graphite is also lower for the beaker cells, indicating a thicker SEI/surface layer on the beaker cell electrodes. For the beaker cells, there might be some differences between the stacked and side-by-side configuration. However, this cannot be concluded based on this work alone since charging is suspected for the electrode cycled in the side-by-side configuration. Furthermore, for the LFP no significant differences can be observed between the electrodes cycled in different configurations. This means that it is possible that the electrode placement affects the surface composition of the graphite, but not the surface composition of the LFP. As with the electrochemical performance, the observed differences between the two beaker cells and the coin cell could however be related to the open cell configuration or the electrolyte volume as opposed to the electrode placement.

Chapter 7

Conclusion and Outlook

This thesis project investigated the role of electrode placement in cells used for operando and in situ AP-XPS experiments. This was done by comparing two beaker cell configurations, with a side-by-side and a stacked electrode placement, as well as a coin cell configuration. The galavanostatic cycling showed differences in the voltage curves between the beaker cells and the coin cell which indicates different LFP phase transition pathways. The lower discharge capacities of the beaker cells also indicate an overall worse electrochemical performance for the beaker cells. Furthermore, EIS experiments suggest that the resistances increase with distance between the electrodes as the stacked electrode placement showed the highest electrolyte and charge transfer resistance. However, it should be noted the measurements were carried out without a reference electrode, which might affect the results. For the surface composition of the graphite electrode, XPS measurements demonstrate that the electrodes cycled in beaker cells have a higher concentration of salt-derived elements (F, P, and Li) and a lower concentration of solvent-derived elements (C and O) compared to the coin cell electrode after cycling. The differences in chemical species between the two beaker cells could not be reliably compared due to unusual spectral shapes for the side-by-side cell possible caused by differential charging. For the surface composition of the cycled LFP electrodes, no significant differences can be observed between the different configurations. These results show that is is possible that the electrode placement plays a role in the surface composition of graphite. However, the observed differences could also be a result of the difference in electrolyte volume. For the LFP, no differences could be observed between the different cells during the first charge-discharge cycle.

The results of this work have shown that the electrode placement can possibly affects the electrochemical reactions, electrode surface composition and resistances in LIBs. However, other aspects could influence these results, such as the open cell configuration of the beaker cells and the differences in electrolyte volume between the beaker cells and the coin cell. This knowledge should be taken into account when dip-and-pull experiments are performed. This work has also presented a new design for the sample holder for dip-and-pull AP-XPS experiments that will enable measurements on both the positive and negative electrode. The project has therefore contributed to the field of AP-XPS by allowing for new AP-XPS experiments, where both the positive and negative electrode can be probed. It has also contributed to the field by showcasing that the results obtained with a dip-and-pull setup cannot necessarily be directly transferred to a more realistic battery.

To continue this project, EIS measurement with a three-electrode setup should be carried out to validate the interpretation of the resistances. Furthermore, additional post-mortem XPS on the graphite electrode in the side-by-side configuration should be performed more carefully to confirm or invalidate the unusual spectra obtained previously. Future work should also include investigating the performances of the beaker cell setups in a pulled-up state. This should encompass testing if a common meniscus can be created in the side-by-side setup. Finally, dip-and-pull experiments with the new sample holder should be performed, both to compare its performance to the stacked sample holder and to utilize its ability to probe both the positive and negative electrode.

Acknowledgements

I would first like to thank my supervisor Auðunn Orri Elvarsson for making this thesis project so enjoyable and instructive. I would not have learnt half as much if I did not have a supervisor as invested as you. I would also like to thank my examiner Julia Maibach for introducing me to the world of AP-XPS and for the guidance you have given me throughout this project.

Thank you also to Rob Temperton for answering all my questions about the HIPPIE sample holder and to Ezio Zanghellini for all the help and support in the lab as well as for accommodating my unconventional experimental setups. I also want to thank Jan-Åke Wiman for valuable discussions about the design of the sample holder. To Simon Lindberg, thank you for helping me make some sort of sense of the EIS data.

This experience would also not have been the same without all of the fantastic people I have met at MF. Thank you all for being so generous with your knowledge and experience. Although I have loved my project, the lunches and fika with you have been the best part of my time at the division.

I would also like to thank my family for all the love and support I have received. And to Gabriel, thank you for being the safe space I can come home to after a long day.

Bibliography

[1] The International Energy Agency. *Electricity consumption.* URL: `https://www.iea.org/reports/electricity-information-overview/electricity-consumption`. (accessed: 19.03.2026).

[2] The International Energy Agency. *Electricity.* URL: `https://www.iea.org/reports/global-energy-review-2025/electricity`. (accessed: 18.03.2026).

[3] Cynthia Kuo, Craig Lindberg, and David J. Thomson. “Coherence established between atmospheric carbon dioxide and global temperature”. In: *Nature* 343 (1990), pp. 709–714. DOI: `https://doi.org/10.1038/343709a0`.

[4] G. Foster and S. Rahmstorf. “Global Warming Has Accelerated Significantly”. In: *Geophys Res Lett* 53.5 (2026). DOI: `https://doi.org/10.1029/2025GL118804`.

[5] Triana Wulandari et al. “Lithium-based batteries, history, current status, challenges, and future perspectives”. In: *Battery Energy* 2.6 (2023). DOI: `https://doi.org/10.1002/bte2.20230030`.

[6] The Nobel Prize. *Nobel Prize in Chemistry 2019.* URL: `https://www.nobelprize.org/prizes/chemistry/2019/summary/`. (accessed: 18.03.2026).

[7] Robert A. Huggins. *Advanced Batteries.* Springer, Boston, MA, 2009. Chap. Introductory Material. DOI: `https://doi.org/10.1007/978-0-387-76424-5_1`.

[8] Wajid Ali et al. “A comprehensive review on coating techniques to suppress the dendrites issue and improve the performance of lithium-ion batteries”. In: *Journal of Coatings Technology and Research* 22 (2025), pp. 1433–1450. DOI: `https://doi.org/10.1007/s11998-024-01050-y`.

[9] Walid Dachraoui et al. “Nucleation, growth and dissolution of Li metal dendrites and the formation of dead Li in Li-ion batteries investigated by operando electrochemical liquid cell scanning transmission electron microscopy”. In: *Nano Energy* 130 (2024). DOI: `https://doi.org/10.1016/j.nanoen.2024.110086`.

[10] Wenjing Zhang et al. “Insights into dendrite penetration induced short circuit failures in lithium-ion batteries: An electro-chemo-thermal coupled phase-field approach”. In: *Journal of Energy Storage* 149 (2026). DOI: `https://doi.org/10.1016/j.est.2025.120322`.

[11] Jianmin. Ma. *Liquid Electrolyte Chemistry for Lithium Metal Batteries - Design, Mechanisms, Strategiess.* John Wiley & Sons, 2022. Chap. Electrode–Electrolyte Interphase. URL: `https://app.knovel.com/hotlink/toc/id:kpLECLMBD1/liquid-electrolyte-chemistry/liquid-electrolyte-chemistry`.

[12] Satu Kristiina Heiskanen, Jongjung Kim, and Brett L. Lucht. “Generation and Evolution of the Solid Electrolyte Interphase of Lithium-Ion Batteries”. In: *Joule* 3.10 (2019). DOI: `https://doi.org/10.1016/j.joule.2019.08.018`.

[13] E. Peleda, D. Golodnitsky, and G. Ardel. “Advanced Model for Solid Electrolyte Interphase Electrodes in Liquid and Polymer Electrolytes”. In: *Journal of The Electrochemical Society* 144.8 (1997). DOI: `10.1149/1.1837858`.

[14] S. Malmgren et al. “Comparing anode and cathode electrode/electrolyte interface composition and morphology using soft and hard X-ray photoelectron spectroscopy”. In: *Electrochimica Acta* 97 (2013), pp. 23–32. DOI: `10.1016/j.electacta.2013.03.010`.

[15] Junxiong Wu et al. “Understanding solid electrolyte interphases: Advanced characterization techniques and theoretical simulations”. In: *Nano Energy* 89.part B (2021). DOI: `https://doi.org/10.1016/j.nanoen.2021.106489`.

[16] Yaolin Xu et al. “Promoting Mechanistic Understanding of Lithium Deposition and Solid-Electrolyte Interphase (SEI) Formation Using Advanced Characterization and Simulation Methods: Recent Progress, Limitations, and Future Perspectives”. In: *Advanced Energy Materials* 12.19 (2022). DOI: `https://doi.org/10.1002/aenm.202200398DigitalObjectIdentifier(DOI)`.

[17] The Nobel Prize. *Nobel Prize in Physics 1921*. URL: `https://www.nobelprize.org/prizes/physics/1921/summary/`. (accessed: 01.04.2026).

[18] Edward L. Alpen. *Radiation Biophysics (Second Edition)*. Academic Press, 1998, pp. 27–49. ISBN: 9780120530854. DOI: `https://doi.org/10.1016/B978-012053085-4/50005-3`.

[19] M. H. Kibel. *Surface Analysis Methods in Materials Science*. Springer Series in Surface Sciences, vol 23. Springer, Berlin, Heidelberg, 2003. Chap. X-Ray Photoelectron Spectroscopy. ISBN: 978-3-662-05227-3.

[20] *EA 125 Energy Analyser*. 2.1. omicron nanotechnology. 2002.

[21] Grzegorz Greczynski and Lars Hultman. “A step-by-step guide to perform x-ray photoelectron spectroscopy”. In: *Journal of Applied Physics* 132.1 (2022). DOI: `https://doi.org/10.1063/5.0086359`.

[22] A.S. Racz and M. Menyhard. “Evaluation methods for XPS depth profiling; A review”. In: *Applied Surface Science Advances* 30 (2025). DOI: `https://doi.org/10.1016/j.apsadv.2025.100872`.

[23] Ingvar Lindgren. “Chemical shifts in X-ray and photo-electron spectroscopy: a historical review”. In: *Journal of Electron Spectroscopy and Related Phenomena* 137-140 (2004), pp. 59–71. DOI: `https://doi.org/10.1016/j.elspec.2004.02.086`.

[24] Mark C. Biesinger. “Advanced analysis of copper X-ray photoelectron spectra”. In: *Surface and Interface Analysis* 49.13 (2017). DOI: `https://doi.org/10.1002/sia.6239`.

[25] Mark H. Engelhard et al. “Introductory guide to backgrounds in XPS spectra and their impact on determining peak intensities”. In: *J. Vac. Sci. Technol. A* 38.6 (2020). DOI: `https://doi.org/10.1116/6.0000359`.

[26] Hans Siegbahn and Kai Siegbahn. “ESCA applied to liquids”. In: *Journal of Elecfron Spec froscopy and Related Phenomena* 2.3 (1973), pp. 319–325. DOI: `https://doi.org/10.1016/0368-2048(7)380023-4`.

[27] Rosemary Jones et al. “Multimodal Ambient Pressure Sample Environment for the HIPPIE Solid-Gas Endstation at MAX IV Laboratory”. In: *Photon Science* 1.2 (2025), pp. 111–120. DOI: `https://doi.org/10.1021/photonsci.5c00021`.

[28] Julia Maibach et al. “Toward Operando Characterization of Interphases in Batteries”. In: *ACS Materials Lett.* 5.9 (2023), pp. 2431–244. DOI: `https://doi.org/10.1021/acsmaterialslett.3c00207`.

[29] Ida Källquist et al. “Probing Electrochemical Potential Differences over the Solid/Liquid Interface in Li-Ion Battery Model Systems”. In: *ACS Appl. Mater. Interfaces* 13.28 (2021), pp. 32989–32996. DOI: `https://doi.org/10.1021/acsami.1c07424`.

[30] Qianhui Liu et al. “Operando APXPS for direct probing of Li ion battery LCO electrode/electrolyte interface chemistry during lithiation/delithiation”. In: *J. Mater. Chem. A* 13 (2025), pp. 20568–20577. DOI: `https://doi.org/10.1039/D5TA01654A`.

[31] F. G. Capone et al. “Operando observation of the dynamic SEI formation on a carbonaceous electrode by near-ambient pressure XPS”. In: *Energy Environ. Sci.* 17 (2024), pp. 1509–1519. DOI: `https://doi.org/10.1039/D3EE03228K`.

[32] Alenka Križan et al. “Impact of mass transport on meniscus electrochemistry determined by time-resolved operando X-ray photoelectron spectroscopy”. In: *Physical Chemistry Chemical Physics* 27 (2025), pp. 7456–7466. DOI: `https://doi.org/10.1039/D5CP00168D`.

[33] Bernadette Davies et al. “Insight into the Carbon Monoxide Reduction Reaction on Cu(111) from Operando Electrochemical X-ray Photoelectron Spectroscopy”. In: *Angewandte Chemie International Edition* 64.33 (2025). DOI: `https://doi.org/10.1002/anie.202506402`.

[34] Oh B. Chae, Jongjung Kim, and Brett L. Lucht. “Modification of lithium electrodeposition behavior by variation of electrode distance”. In: *Journal of Power Sources* 532 (2022), p. 231338. DOI: `https://doi.org/10.1016/j.jpowsour.2022.231338`.

[35] Helena Berg. *Batteries for Electric Vehicles. Materials and Electrochemistry.* Cambridge university press, 2015. ISBN: 978-1-107-08593-0.

[36] Alexandros Ch. Lazanas and Mamas I. Prodromidis. “Electrochemical Impedance SpectroscopyA Tutorial”. In: *ACS Measurement Science Au* 3.3 (2023), pp. 162–193. DOI: `https://doi.org/10.1021/acsmeasuresciau.2c00070`.

[37] Seong Jin An et al. “The state of understanding of the lithium-ion-battery graphite solid electrolyte interphase (SEI) and its relationship to formation cycling”. In: *Carbon* 105 (2016), pp. 52–76. DOI: `https://doi.org/10.1016/j.carbon.2016.04.008`.

[38] Jianfeng Jia et al. “Relaxation-Induced Memory Effect of LiFePO4 Electrodes in Li-Ion Batteries”. In: *ACS Applied Materials Interfaces* 9.29 (2017), pp. 24561–24567. DOI: `https://doi.org/10.1021/acsami.7b0585`.

[39] Victoria A. Nikitina and Stanislav S. Fedotov. “Solvent control of the nucleation-induced voltage hysteresis in Li-rich LiFePO4 materials”. In: *Electrochimica Acta* 437 (2023), p. 141503. DOI: `https://doi.org/10.1016/j.electacta.2022.141503`.

[40] Xiaolong Guo et al. “Size-Dependent Memory Effect of the LiFePO4 Electrode in Li-Ion Batteries”. In: *ACS Applied Materials Interfaces* 10.48 (2018), pp. 41407–41414. DOI: `https://doi.org/10.1021/acsami.8b15933`.

[41] Ikuma Takahashi et al. “Irreversible phase transition between LiFePO4 and FePO4 during high-rate charge-discharge reaction by operando X-ray diffraction”. In: *Journal of Power Sources* 309 (2016), pp. 122–126. DOI: `https://doi.org/10.1016/j.jpowsour.2016.01.077`.

[42] Vijay A. Sethuraman et al. “Surface structural disordering in graphite upon lithium intercalation/deintercalation”. In: *Journal of Power Sources* 195 (2010), pp. 3655–3660. DOI: `https://doi.org/10.1016/j.jpowsour.2009.12.034`.

[43] Yoshinao Hoshi et al. “Optimization of reference electrode position in a three-electrode cell for impedance measurements in lithium-ion rechargeable battery by finite element method”. In: *Journal of Power Sources* 288 (2015), pp. 168–175. DOI: `https://doi.org/10.1016/j.jpowsour.2015.04.065`.

[44] Nicolo’ Comini et al. “Factors influencing surface carbon contamination in ambient-pressure x-ray photoelectron spectroscopy experiments”. In: *journal of vacuum science technology a* 39.4 (2021). DOI: `https://doi.org/10.1116/6.0001013`.

[45] Jeng-Ywan Shih et al. “Operando investigation on the fast two-phase transition kinetics of LiFePO4/C composite cathodes with carbon additives for lithium-ion batteries”. In: *Electrochimica Acta* 419.140356 (2022). DOI: `https://doi.org/10.1016/j.electacta.2022.140356`.

Appendix A

Supplementary Information

A.1 Galvanostatic cycling

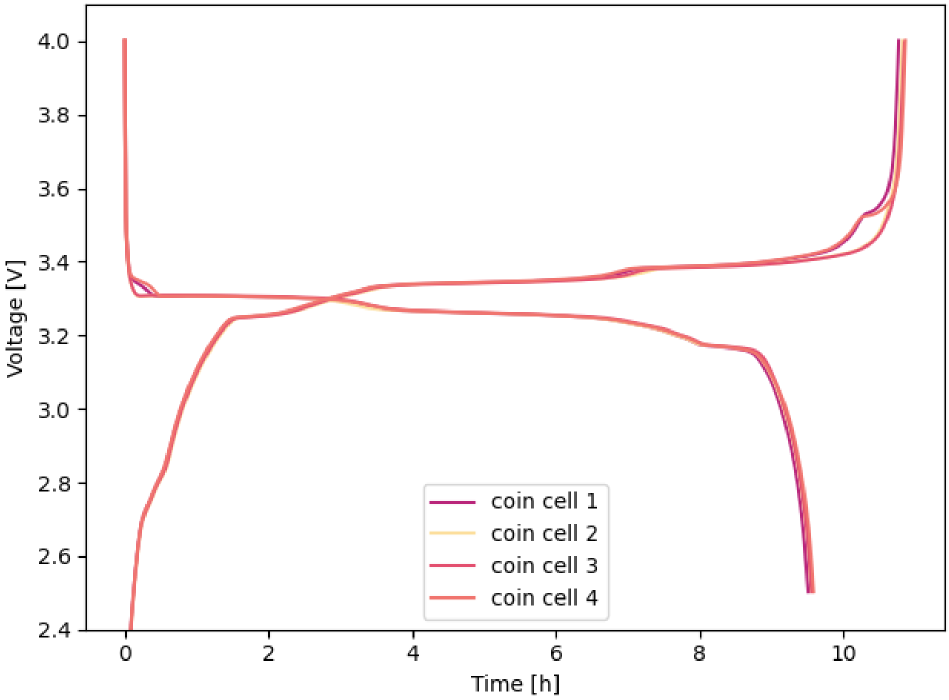

Figure A.1: Galvanostatic charge/discharge of all coin cells. The charging curves start in the bottom left and end in the upper right corner, while the discharge curves start in the upper left and end in the lower right corner.

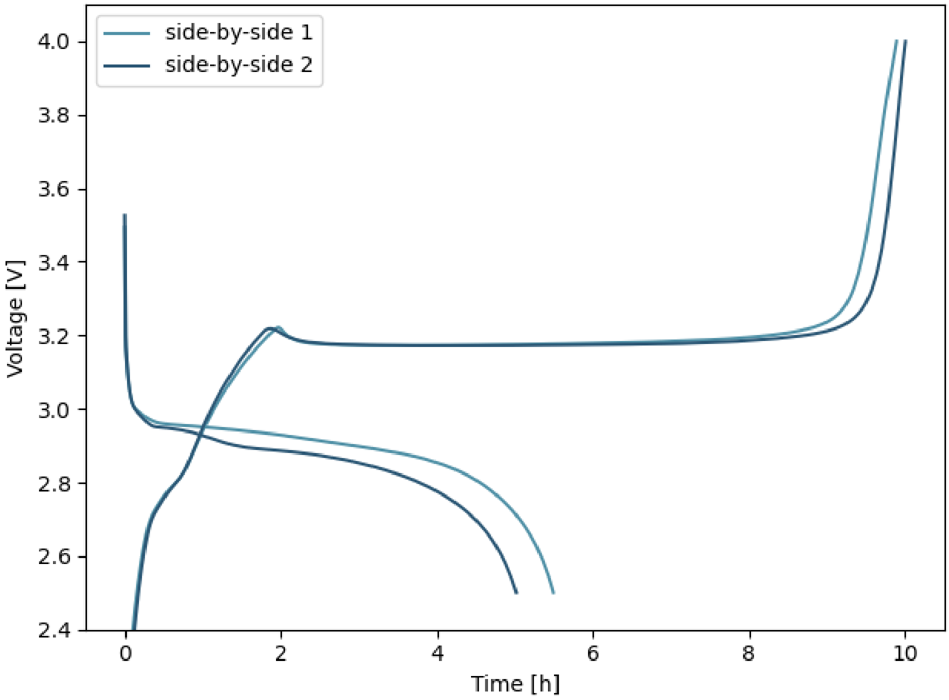

Figure A.2: Galvanostatic charge/discharge of all beaker cells with a side-by-side electrode placement. The charging curves start in the bottom left and end in the upper right corner, while the discharge curves start in the upper left and end in the lower right corner.

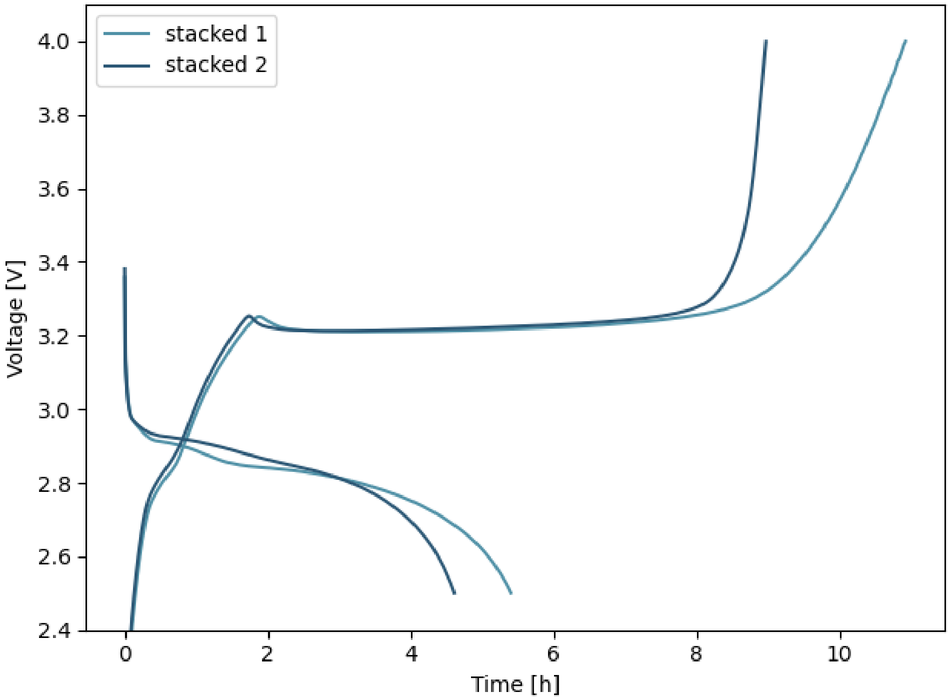

Figure A.3: Galvanostatic charge/discharge of all beaker cells with a stacked electrode placement. The charging curves start in the bottom left and end in the upper right corner, while the discharge curves start in the upper left and end in the lower right corner.

A.2 Electrochemical Impedance Spectroscopy

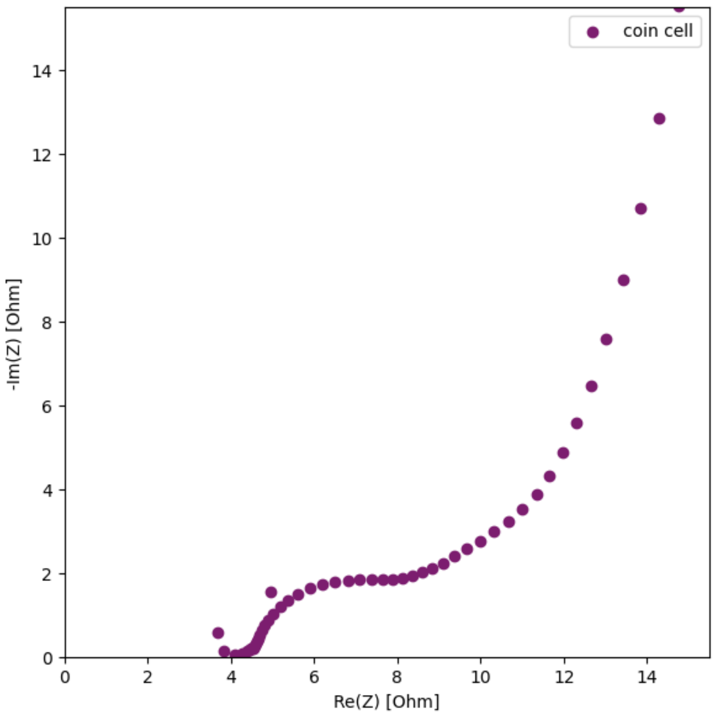

Figure A.4: EIS obtained with the coin cell configuration.

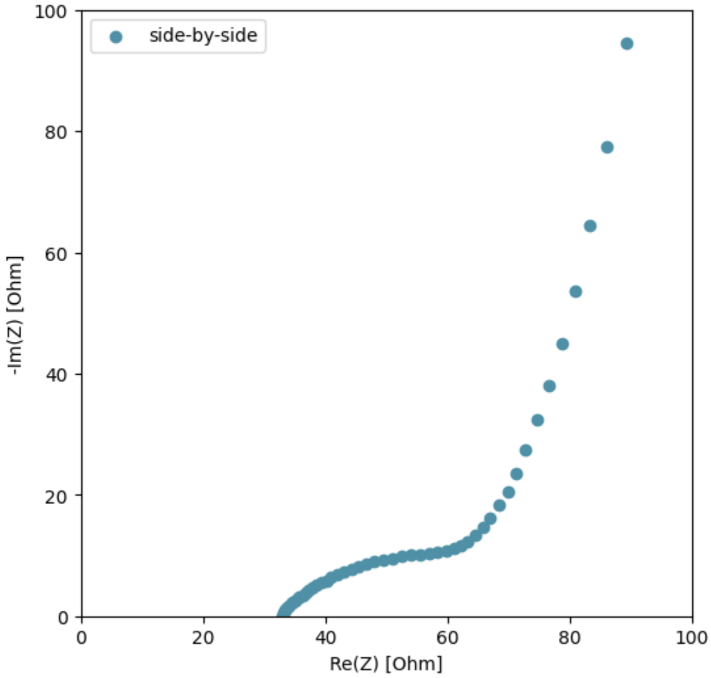

Figure A.5: EIS obtained with the side-by-side configuration.

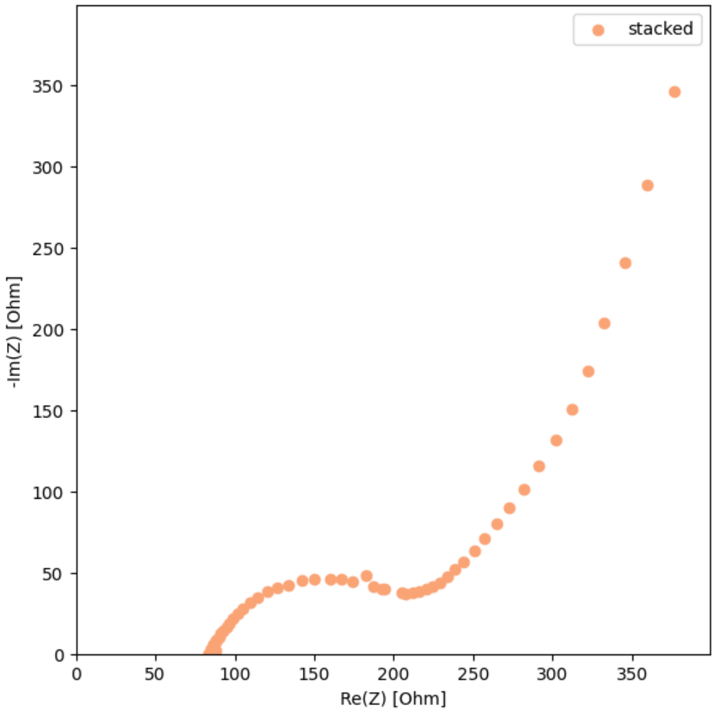

Figure A.6: EIS obtained with the stacked configuration.

A.3 X-ray Photoelectron Spectroscopy

Table A.1: Relative sensitivity factor (RSF) of different elements.

Element	F 1s	O 1s	C 1s	P 2p	Li 1s	Fe 2p
RSF	3.23	2.36	1	1.91	0.0883	2.686

CHALMERS UNIVERSITY OF TECHNOLOGY
Gothenburg, Sweden 2026
www.chalmers.se